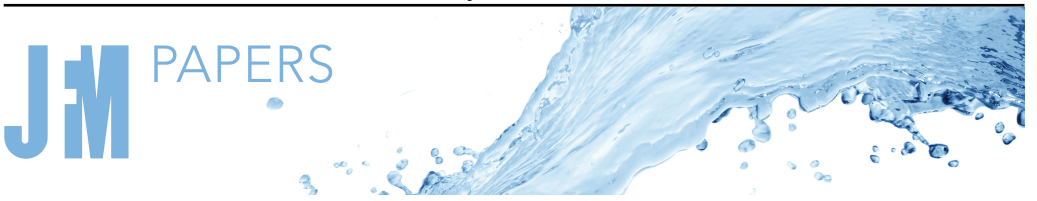
J. Fluid Mech. (2025), *vol.* 1024, A24, doi:10.1017/jfm.2025.10866



The effect of structural damping on the flow-induced vibration of an elastically mounted oblate spheroid

Adrian Cordero Obando[1], **Mark C. Thompson**[1], **Kerry Hourigan**[1] and **Jisheng Zhao**[1,2]

[1]Fluids Laboratory for Aeronautical and Industrial Research (FLAIR), Department of Mechanical and Aerospace Engineering, Monash University, Clayton, VIC 3800, Australia

[2]School of Engineering and Technology, University of New South Wales, Canberra, ACT 2600, Australia

Corresponding author: Adrian Cordero Obando, adrian.corderoobando@monash.edu

(Received 4 June 2025; revised 8 September 2025; accepted 21 October 2025)

This paper presents an experimental investigation focusing on the impact of structural damping on the flow-induced vibration (FIV) of a set of generic three-dimensional bodies, in this case, elastically mounted oblate spheroids. The objective is to identify and analyse the two primary FIV responses: vortex-induced vibration (VIV) and galloping, and how these vary with structural damping ratio. The VIV response has similarities to that observed for a sphere, reaching a maximum amplitude of approximately one major diameter. However, and not seen in the sphere case, a galloping-like response exhibits a linear amplitude growth as the reduced velocity is increased beyond the normal resonant range, akin to the transverse galloping response seen for a D-section or elliptical cross-section cylinder. By increasing the damping ratio, this aerodynamic-instability-driven response is effectively suppressed. However, increased damping also significantly reduces the VIV response, decreasing its maximum amplitude and contracting the VIV synchronisation, or lock-in, region. These results suggest that three-dimensional spheroids, as for two-dimensional cylindrical bodies such as D-section and elliptical cylinders, can encounter asymmetric aerodynamic forces that support movement-induced vibration, resulting in substantial body oscillation – beyond that expected under VIV alone. The study indicates that modifying the structural damping ratio can facilitate a transition between the VIV and galloping responses. These findings offer novel insights into the dynamics of fluid–structure interactions and have potential implications for designing structures and devices that can experience resonant flow conditions. Additionally, the energy harvesting performance of oblate spheroids has been evaluated, revealing that

© The Author(s), 2025. Published by Cambridge University Press. This is an Open Access article, distributed under the terms of the Creative Commons Attribution licence (https://creativecommons.org/licenses/by/4.0/), which permits unrestricted re-use, distribution and reproduction, provided the original article is properly cited.

https://doi.org/10.1017/jfm.2025.10866 Published online by Cambridge University Press

the afterbody significantly influences energy harvesting capabilities. Notably, an oblate spheroid can extract up to 50 % more power from the fluid flow than a sphere.

Key words: flow-structure interactions, vortex shedding, wakes

1. Introduction

Fluid–structure interaction (FSI) is a fascinating area of study that explores the complex interplay between a fluid and a structural component. One crucial facet of FSI is flow-induced vibration (FIV), which plays a significant role in the design of engineered structures, such as bridges, ocean platforms, and wind turbine blades, amongst others (Hourigan *et al.* 2026). FIV is a dual-nature phenomenon: it can cause undesirable long-term fatigue, leading to structural failure, but it also holds the potential as a renewable energy source. This duality makes FIV a topic of considerable interest and importance.

Research into characterising and controlling FIV has a rich history (e.g. Choi, Jeon & Kim 2008; Williamson & Govardhan 2008; Wang *et al.* 2020*b*). Understanding the fundamental mechanisms behind structural vibration and being able to control the vibration has resulted in innovative methods to extract energy from fluid–structure systems (e.g. Wang *et al.* 2020*a*; Lv *et al.* 2021). Interestingly, studies suggest that the energy-harvesting performance of an elastically mounted bluff body can be enhanced through optimising damping ratio (see Soti *et al.* 2017, 2018) and can be significantly affected by body rotation (see Wang *et al.* 2017; Zhao *et al.* 2022*a*). However, apart from spheres, FIV of three-dimensional (3-D) bluff bodies has not received much attention. This existing gap presents opportunities to explore FIV of oblate spheroids.

Two body-oscillator phenomena are of particular interest for this investigation: Vortex-induced vibration (VIV), categorised as an instability-induced excitation (IIE), and galloping, categorised as a movement-induced excitation (MIE) (see Naudascher & Rockwell 2005). VIV generally occurs for elastic or elastically mounted bluff bodies (often a circular cylinder or sphere) immersed in a free stream flow. When the vortex-shedding frequency is close to the body oscillation frequency, the separating shear layers and the wake vortices generate a fluctuating pressure distribution on the surface of the body, sustaining a resonance between the system frequency and shedding frequency over specific flow velocity ranges.

The most significant excitation in cross-flow vibrations occurs near the resonance (or synchronisation) condition, $f_y \cong f_{vo} \cong f_{nw}$, i.e. $f^* \equiv f/f_{nw} \cong 1$, where f_y, f_{vo} and f_{nw} denote the body vibration frequency, the vortex shedding frequency and the natural frequency of the structural system in quiescent working fluid, respectively. However, harmonic or subharmonic frequency synchronisations may also contribute to excitation when f is an integer multiple of f_y (harmonic) or when f_y is an integer multiple of f (subharmonic). Examples of harmonic synchronisation have been observed in the FIV of square and D-section cylinders (Zhao *et al.* 2014*b*, 2018*a*), while subharmonic synchronisation has been revealed for square cylinders placed at an incidence angle of 20° (Nemes *et al.* 2012; Zhao *et al.* 2014*b*, 2018*c*). The physical origin of these harmonic or subharmonic synchronisations stem from the influence of the afterbody geometry on vortex formation, where the afterbody manifests the vortex shedding process and fluid–structure frequency synchronisation – vortices may be shed at frequencies higher or lower than the body vibration frequency. In synchronisation or the lock-in regime, the vortex shedding frequency typically deviates from the Strouhal frequency relationship,

https://doi.org/10.1017/jfm.2025.10866 Published online by Cambridge University Press

$f_{St} = StU/b$, for a fixed body, where St is the Strouhal number (see Bearman 1984). Structural damping plays a crucial role in controlling vibration amplitude and lock-in range. Increasing the structural damping ratio (ζ) significantly reduces both the maximum vibration amplitude and the lock-in range width (e.g. Soti *et al.* 2018; Lo *et al.* 2023).

In the late 1990s, Williamson & Govardhan (1997) and Govardhan & Williamson (1997) conducted pioneering studies on a tethered sphere subject to two degrees-of-freedom (DOF). They characterised its dynamic response by plotting the amplitude of vibration as a function of a dimensionless velocity called reduced velocity, defined by $U^* = Ub/f_{nw}$, where U is the free stream velocity. Two distinct modes of vortex formation were identified, named modes I and II, over the range of reduced velocities $U^* \in [0, 20]$. The vortex shedding frequency, f_{vo}, of these two modes remained close to the natural frequency of the system, $f^* = f_{vo}/f_{nw} \sim 1$, indicating a resonant VIV response.

Further investigation by Govardhan & Williamson (2005) analysed the dynamic response of an elastically mounted sphere, subject to only cross-flow oscillation, as well as the tethered sphere configuration. For both cases, they found that the two vibration modes occur over a synchronisation (i.e. lock-in) region where the vortex shedding frequency locks onto the natural frequency of the system. They showed that the mass-damping parameter, $(m^* + C_A)\zeta$, or Scruton number, $Sc = 2m\zeta/(\rho b^2)$, plays a vital role in determining the details of the dynamic response of the bluff body; here, m^* is the mass ratio, defined as the ratio of the total oscillating mass, m, to the fluid mass displaced by the body, m_d, namely $m^* = m/m_d$; ζ is the damping ratio; and C_A is the added-mass coefficient. In particular, an increase in $(m^* + C_A)\zeta$ causes a narrowing of the synchronisation range and a reduction in the maximum amplitude of vibration.

For spheres that are denser than the fluid, i.e. $m^* > 1$, the FIV response transitions smoothly between VIV modes I and II, which makes it difficult to quantify the boundary between the modes just by looking at the body vibration response varying with reduced velocity. Hence, to distinguish the range of reduced velocity associated with each mode, they analysed the variation of the total phase, ϕ_t, defined as the phase angle difference between the total transverse fluid force, F_y, and the sphere displacement, y, and the vortex phase, ϕ_v, defined as the phase angle difference between the vortex force component, F_v, and y. When analysing the fluid forcing on a bluff body constrained to single-degree-of-freedom motion in either cross-flow or streamwise directions, the total force can be decomposed into two distinct contributions: potential (inviscid) and vortical (viscous) components; e.g. $F_y = F_p + F_v$, with F_p being the potential force (see Govardhan & Williamson 2000). The potential force stems from the inertial effects of fluid acceleration around the moving body, also known as the added-mass effect, which manifests as a force proportional to body acceleration in potential flow theory; e.g. $F_p = -m_A\ddot{y}$, with $m_A = C_A m_d$ being the added mass. The vortex force (viscous contribution) originates from the unsteady vortical structures in the body's wake, representing the effects of rotational flow that complement the contribution by the irrotational potential flow (see Lighthill 1986; Govardhan & Williamson 2000; Limacher, Morton & Wood 2018; Limacher 2021; Zhao *et al.* 2022*b*). Digital particle image velocimetry (DPIV) was undertaken to elucidate the difference between modes I and II; both modes were shown to consist of hairpin-like vortex loops, with the main difference being the timing of vortex loop formation. This was later corroborated by Sareen *et al.* (2018*a*), Eshbal *et al.* (2019*a*) and Kovalev, Eshbal & van Hout (2022), who observed similar wake patterns for elastically mounted and tethered spheres.

In addition to Mode I and Mode II, Jauvtis, Govardhan & Williamson (2001) identified Mode III, characterised by periodic vibration occurring for high reduced velocities over the range $U^* \in [20, 40]$. Within this vibration regime, the vortex shedding frequency was three to eight times higher than the natural frequency of the sphere, suggesting that the

https://doi.org/10.1017/jfm.2025.10866 Published online by Cambridge University Press

classical 'lock-in' theory cannot explain the vibration mechanism. Instead, Govardhan & Williamson (2005) associated Mode III with MIE, arguing that Mode III is suppressed in the absence of body movement; however, the elastically mounted, or tethered, sphere is intrinsically unstable and if the body is perturbed, a self-sustaining vortex force can be generated to amplify the body vibration to potentially large amplitudes. It is noteworthy that Mode III appears to be different from conventional galloping and this mode has been observed only in tethered or elastically mounted spheres. Rajamuni, Thompson & Hourigan (2020) conducted a direct numerical simulation (DNS) of a freely vibrating tethered sphere ($m^* > 1$) and identified Mode III as an unstable vibration mode from simulations at Reynolds numbers up to 2000.

Jauvtis *et al.* (2001) also experimented with very high reduced velocities ($U^* \geqslant 100$) for a tethered sphere in a wind tunnel and found a fourth mode of vortex formation characterised by intermittent bursts, resulting in non-periodic oscillations. The vibration frequency remained close to the natural shedding frequency of the sphere, in contrast to Mode III. Conversely, for the case of a light sphere, Rajamuni *et al.* (2020) reported that Mode II was followed by a non-periodic Mode IV response at low reduced velocities, without the appearance of Mode III.

Galloping, a body oscillator phenomenon typical of FIV that does not occur for rotationally symmetric bodies such as circular cylinders and spheres, was initially investigated because of its occurrence with ice-covered electric transmission lines (Den Hartog 1932). The low-frequency, large-amplitude displacement waves along the lines gave rise to the name. This mechanism is characterised by a continuous (almost linear) increase in vibration amplitude above a critical reduced velocity threshold value, U^*_{crit}. Galloping represents a classical aerodynamic instability in that transverse body motion creates an aerodynamic force that enhances the motion of the body. Extensive research has been conducted on the vibration mechanism using the canonical case of a square cross-section or D-section cylinder (Parkinson & Smith 1964; Bearman *et al.* 1987; Blevins 2001; Zhao *et al.* 2014*a*).

Galloping occurs in flows characterised by separated shear layers that do not reattach to the trailing edge of a body at rest. In such cases, movement-induced excitation arises without a phase shift between fluid forces and body velocity, with forces closely matching those predicted by quasi-steady conditions. Galloping is common for short bluff bodies in cross-flow, particularly when the length-to-height ratio is small. This instability requires only one degree of freedom and can be theoretically predicted using the transverse force coefficient (C_y) as a function of the angle of attack (α), derived from the drag and lift coefficients (C_D and C_L). The onset of galloping is highly sensitive to changes in geometry, as minute deviations in shape can drastically alter C_D and C_L, leading to unpredictable behaviour. As shown by Cheng *et al.* (2023), altering the windward interior angle of an elastically mounted isosceles-trapezoidal cross-section by $\sim 1^\circ$ from 90° could either significantly amplify or completely suppress galloping. Examples include cables in cross-flow affected by ice formation, marine organisms or rainwater, which can induce instabilities even at low free stream velocities (e.g. $450\,\mathrm{mm\,s^{-1}}$) and result in large vibration amplitudes (up to 10 m). Susceptibility to galloping can often be tested by imagining the structure displaced from equilibrium with velocity $\dot{y} = \partial y/\partial t$, analysing the resulting flow changes in a quasi-steady manner.

Studies involving elastically mounted or tethered spheres have not reported a typical galloping response, which is consistent with their rotational symmetry. However, Sareen *et al.* (2018*a*) and McQueen *et al.* (2020) have demonstrated that imposing rotation on an elastically mounted sphere, and thus breaking the symmetry, induces galloping-like oscillations. In this case, the amplitude of vibration response increases continually beyond

https://doi.org/10.1017/jfm.2025.10866 Published online by Cambridge University Press

a critical U^* value. Nonetheless, contrary to classical galloping, the high-amplitude vibrations occur at low reduced velocities, with the body displacement frequency, f_y^*, being synchronised with the imposed rotation frequency instead of higher harmonics associated with the fluid force frequencies. This vibration regime was termed rotary-induced vibration (RIV), where the vortex shedding in combination with the imposed rotation induces an oscillatory Magnus effect that contributes to the unique behaviour of RIV. Recently, Cordero Obando *et al.* (2024) found that a reduction of the afterbody of a sphere (the part of the sphere beyond the separation line) results in a combined VIV and galloping-like response without an imposed rotation. Thus, VIV and galloping-like responses can occur concurrently or separately, depending on the afterbody geometry, flow conditions (such as Reynolds number) and structural properties (including the mass-damping parameter).

Despite extensive work on two-dimensional (2-D) bluff bodies, there remains a clear gap in understanding how structural properties – most notably the damping ratio – govern the FIV of oblate spheroids. In oblate spheroids, damping can differentially modulate the interplay between VIV-like and galloping-like mechanisms, altering both response amplitude and frequency content. Clarifying this dependence is essential not only for fundamental physics, but also for performance-oriented design. In particular, identifying damping ratios that optimise extractable power would inform FIV-based energy harvesters, analogous to recent advances for circular cylinders (Soti *et al.* 2017; Zhao *et al.* 2022*a*). This perspective motivates the present focus on oblate spheroids and their parameter-dependent dynamics.

Noting these studies, it is reasonable to ask the following questions. (i) What is the vibration response of oblate spheroids relative to that of a sphere? (ii) How does the damping ratio affect the dynamic response of oblate spheroids? The latter is of particular interest for FIV suppression, but also for renewable energy applications, since the available power is a function of damping (applied through a kinetic to electrical energy converter) and the velocity response. There appear to be no readily assessable previous studies on the dynamic response of elastically mounted oblate spheroids as the damping ratio is varied. Thus, the current study aims to investigate, characterise and analyse the FIV response and wake for one degree of freedom (1-DOF) elastically mounted oblate spheroids by exploring the effect of the damping ratio (ζ) as a function of reduced velocity (U^*).

The article is structured as follows. In § 2, we provide an overview of the fluid–structure system modelling and experimental set-up. Section 3 presents the findings and discussion related to the FIV characteristics. Finally, in § 5, we draw conclusions based on the extensive experimental results.

2. Experimental methodology

2.1. *Fluid–structure system*

The governing equation describing the motion of an elastically mounted bluff body undergoing transverse (cross-flow) FIV is given by

$$m\ddot{y} + c\dot{y} + ky = F_y(t), \tag{2.1}$$

where m is the total oscillating mass of the system, c is the structural damping coefficient, k is the spring constant, y is the body displacement and $F_y(t)$ is the time-dependent total transverse fluid force acting on the bluff body. Based on the physical components of this equation, it is possible to define key non-dimensional parameters that determine

https://doi.org/10.1017/jfm.2025.10866 Published online by Cambridge University Press

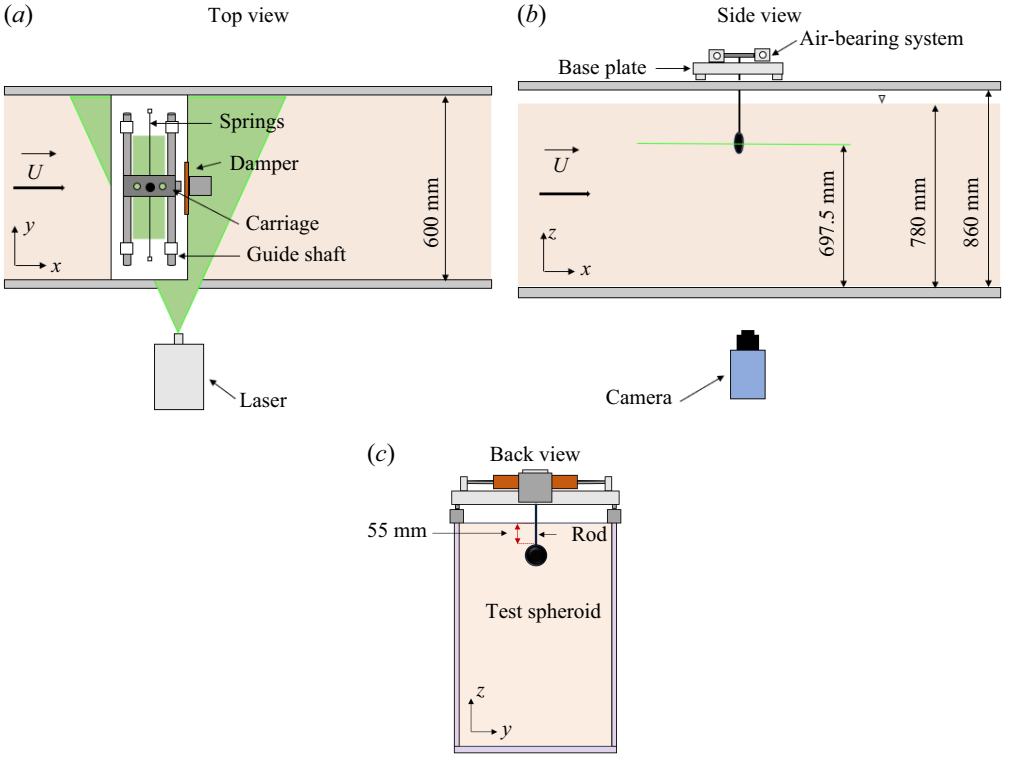


Figure 1. A schematic showing the experimental set-up in (*a*) top view, (*b*) side view and (*c*) back view.

the dynamic response of the system: the mass ratio, the damping ratio and the system oscillation frequency. These are sequentially introduced in the following section.

2.2. *Experimental set-up*

The experiments were conducted in the recirculating water channel of the Fluids Laboratory for Aeronautical and Industrial Research at Monash University, Australia. The dimensions of the test section are 4000 mm in length, 600 mm in width and 800 mm in height (see figure 1 for further details). A low-friction air-bearing rig was used as a part of the hydro-elastic system, constraining the immersed spheroid to oscillate in one direction transversely to the oncoming water flow. Springs attached to both sides of the oscillating mass were used to control the structural stiffness of the system precisely. A more detailed description of the air-bearing system and the water-channel facility can be found from Zhao *et al.* (2018*a*,*b*). An eddy-current damping mechanism was mounted to the air-bearing rig to adjust the net structural damping of the system accurately. Further details on the eddy-current damping device can be found from Soti *et al.* (2017).

The models used for the experiments were precision-machined oblate spheroids made of Renshape 460 (medium–high density polyurethane) with aspect ratios $\epsilon = b/a =$ 1.00, 2.00 and 3.20. The major axis length (cross-stream) was fixed at $b = 50.0$ mm and the different aspect ratios were achieved by varying the minor axis length (streamwise) from $a = 50.0$ mm for the sphere to $a = 16.7$ mm for the $\epsilon = 3.20$ spheroid. The accuracy of these axis lengths was ± 0.20 mm. The main focus of the discussion and analysis is on the $\epsilon = 2.00$ spheroid with the other spheroids used for comparison. The spheroids were supported using a cylindrical support rod of 2.00 mm in diameter, resulting in a

https://doi.org/10.1017/jfm.2025.10866 Published online by Cambridge University Press

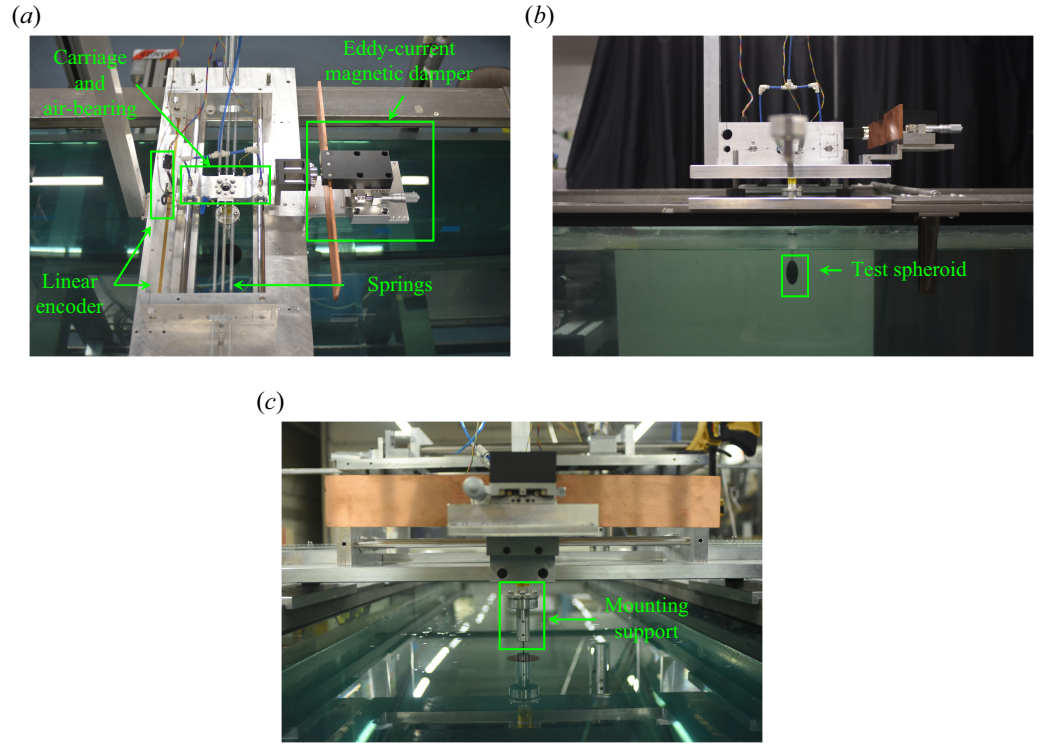


Figure 2. Photographs showing the experimental set-up in (*a*) top view, (*b*) side view and (*c*) back view.

diameter ratio between the spheroid and the support rod of 25. Note that the ratio between the spheroid diameter and rod diameter was based on the major diameters aligned with the cross-flow direction. When the minor diameter aligned with the streamwise direction is considered, this ratio increases substantially. For the case of $\epsilon = 3.20$ (the thinnest spheroid tested), the ratio varied from 7.8 (for the streamwise diameter, $a = 15.6$ mm) to 25.0 (using the cross-flow diameter, $b = 50$ mm). Tomographic-PIV measurements of a sphere supported by a smaller sphere-to-rod diameter ratio of 6 conducted by van Hout *et al.* (2018) demonstrated that the vortex shedding from the rod exhibited at least one order of magnitude lower energy compared with sphere-generated vortex shedding, with no distinct spectral peak associated with the rod in fluid force measurements. Therefore, even for the case of $\epsilon = 3.20$, the effects of the support rod on the FIV response are considered negligible. This configuration adopted the approach established in previous studies of FIV of spheres conducted in the same laboratory (e.g. Sareen *et al.* 2018*a*; McQueen *et al.* 2020). As indicated in figure 1, the immersion length between the spheroid's top to the free surface of the water channel was approximately 55 mm (1.1*b*). This minimised free surface effects on the dynamic response of the immersed body, as shown previously by Mirauda, Volpe Plantamura & Malavasi (2014) and Sareen *et al.* (2018*b*) for the case of spheres of similar size. For $\epsilon = 2.00$, the total oscillating mass of the system was $m = 815.2$ g, comprising the air-bearing carriage, mounting adapters, support rod and spheroid model. The displaced fluid mass was $m_d = (4/3)\pi\rho a^2 b = 32.6$ g, with ρ being the fluid density. This yielded a mass ratio of $m^* = m/m_d \simeq 25$.

Free decay tests were conducted in air and still water to determine the system's natural frequency, with f_{na} the frequency in the air and f_{nw} the frequency in the water. Figure 3 provides the variation of the structural damping ratios, ζ_a (in quiescent air),

https://doi.org/10.1017/jfm.2025.10866 Published online by Cambridge University Press

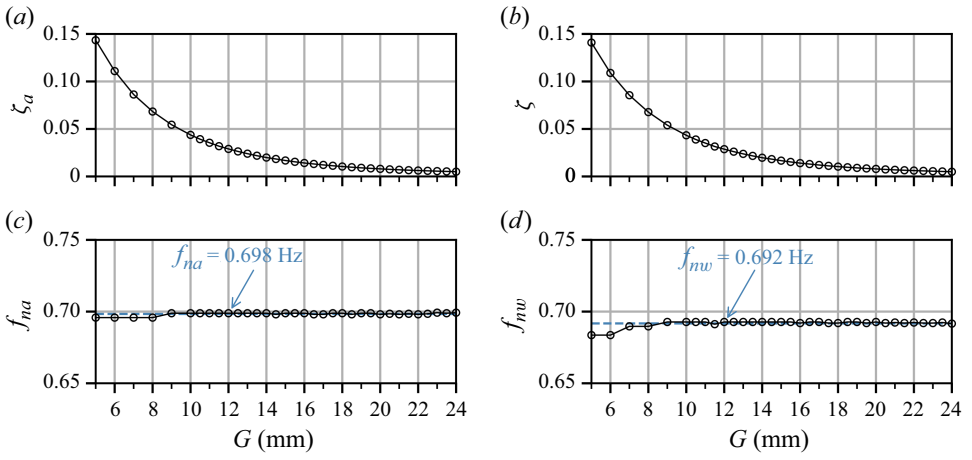


Figure 3. Results of the free-decay tests, presenting the variations of the structural damping ratios and natural frequencies as a function of the damper gap, G. (a) and (c) Outcomes of the structural damping ratio (ζ_a) and the natural frequency (f_{na}) in air, respectively; (b) and (d) Results of the structural damping ratio considering the added mass (ζ) and the natural frequency (f_{nw}) in quiescent water, respectively.

ϵ	b (mm)	a (mm)	m (g)	m_d (g)	m^*	C_A	f_{na} (Hz)	f_{nw} (Hz)
1.00	50.00	50.00	837.50	65.40	12.81	0.590	0.685	0.669
2.00	50.00	25.00	815.10	32.60	25.00	0.446	0.693	0.687
3.20	50.00	15.30	806.10	20.04	39.47	0.349	0.703	0.700

Table 1. Structural properties for the oblate spheroids tested.

and $\zeta = c/(2\sqrt{k(m+m_A)})$ (in quiescent water) with consideration of the fluid added mass, $m_A = ((f_{na}/f_{nw})^2 - 1)m$, and the natural frequencies (f_{na} and f_{nw}), as a function of the gap distance (G) between the magnet and the eddy-current plate of the damper. It can be observed that as the gap distance is increased over the range $5.00 \leqslant G \leqslant 25.00$ mm, the damping ratios decrease following an exponential trend approximately, while the natural frequencies remain almost unchanged, with $f_{na} = 0.693$ Hz and $f_{nw} = 0.687$ Hz. For reference, the structural properties of the spheroids tested are included in table 1. The free-decay test presented in figure 3 is an example for the case $\epsilon = 2.00$ and similar curves were obtained for the other two aspect ratios tested as part of this investigation.

2.3. *Data acquisition and processing methods*

The data were acquired via a computer workstation with LabVIEW (National Instruments, USA) software through a USB data acquisition board (model USB6218-BNC, National Instruments, USA). This also enabled the water-channel flow velocity to be set and sensor measurements to be recorded.

It was crucial to accurately measure the linear displacement to quantify the FIV response of the immersed bluff body. For that purpose, a non-contact digital optical linear encoder (model: RGH24, Renishaw, UK) was installed on the air-bearing rig. The linear encoder has a linear range of 200 mm and can measure displacement with an accuracy of 1 µm. Through numerical differentiation, the recorded displacement was used to determine the instantaneous velocity ($\dot{y}$) and acceleration ($\ddot{y}$), which in turn allowed calculation of the

https://doi.org/10.1017/jfm.2025.10866 Published online by Cambridge University Press

transverse fluid force (i.e. total lift F_y) through the left-hand side of (2.1). This method for determining F_y has been validated by Zhao *et al.* (2014*b*) and Zhao *et al.* (2018*a*). More details of this procedure can be found from Zhao *et al.* (2018*b*). Data were acquired at 100 Hz for each value of reduced velocity and obtained from more than 60 body oscillation cycles after determining that this was sufficient for the asymptotic oscillation amplitude to be reached.

For the measurements of the fluid forces (i.e. transverse lift and drag) for a quasi-steady analysis, the angle of attack of the oblate spheroid was varied and held still using a brushless servo motor (model EC-i40, Maxon Group) equipped with an optical rotary encoder (model ENC 16 RIO with 4096 counts per revolution, Maxon Group) with a resolution of 0.02°. This allowed alignment measurements to be precisely controlled and automated.

To visualise the flow dynamics in the near wake of the immersed oblate spheroid, PIV measurements were undertaken. Micro-spheres of diameter 13 μm and a specific weight of 1.1 g cm^{-3} were added into the flow to quantify planar wake vorticity fields. A laser beam (model MLL-N-532-5W, China) illuminated particles in the equatorial plane (x,y). To capture the wake structure, a high-speed camera (model Dimax S4, PCO AG) with a resolution of 2016 × 2016 pixel^2 and a Nikon lens with a focus length of 50 mm mounted were used. This gave a magnification factor of 5.58 pixel mm^{-1}. To process the images and obtain velocity and vorticity fields, in-house software developed and validated by Fouras, Lo Jacono & Hourigan (2008) was employed. In the present investigation, the imaging of the near wake was done at a sampling rate of 60 Hz for a total of 3000 pairs of images for each dataset. To capture the evolution of the vorticity structures in the wake, the images of each set were divided into 48 phases for averaging, resulting in more than 60 images for each phase bin.

For the majority of the experiments, the reduced velocity range investigated covered $3 \leqslant U^* \leqslant 12$ and the corresponding the Reynolds number range was $4900 \leqslant Re \leqslant 19\,700$.

3. Results and discussion

This section focuses on the dynamic response of the spheroid as a function of reduced velocity. The variation of vibration amplitude with reduced velocity showed distinct vibration regimes over the reduced velocity range examined. The fluid forces and phases were simultaneously recorded to understand the different dynamics controlling the different response regimes. PIV measurements in the wake mid-plane allowed the amplitude response to be connected to the wake flow structures. By varying the damping ratio, the energy harvesting performance of the oblate spheroid could be determined as a function of reduced velocity. However, prior to examining the oblate cases, a presentation and analysis of flow-induced vibration of a sphere, which is been previously studied in some detail (e.g. Govardhan & Williamson 1997, 2000; Sareen *et al.* 2018*a*), is presented to provide validation of the experiments and a reference case for comparison for the oblate bodies.

3.1. *Effect of the mass-damping parameter on the VIV response of a sphere ($\epsilon = 1.00$)*

In this subsection, the dynamic response of an elastically mounted sphere is presented due to its importance to understanding FIV of 3-D bluff bodies. Figure 4(*a*) illustrates the variation of the vibration amplitude, A^*_{10}, as a function of the reduced velocity, U^*, for different values of the mass-damping parameter, $(m^* + C_A)\zeta$. Here, A^*_{10} represents the mean of the top 10 % of amplitude peaks normalised by the major diameter of the sphere, b. It can be clearly seen that for $0.0705 \leqslant (m^* + C_A)\zeta \leqslant 0.5640$, the range of

https://doi.org/10.1017/jfm.2025.10866 Published online by Cambridge University Press

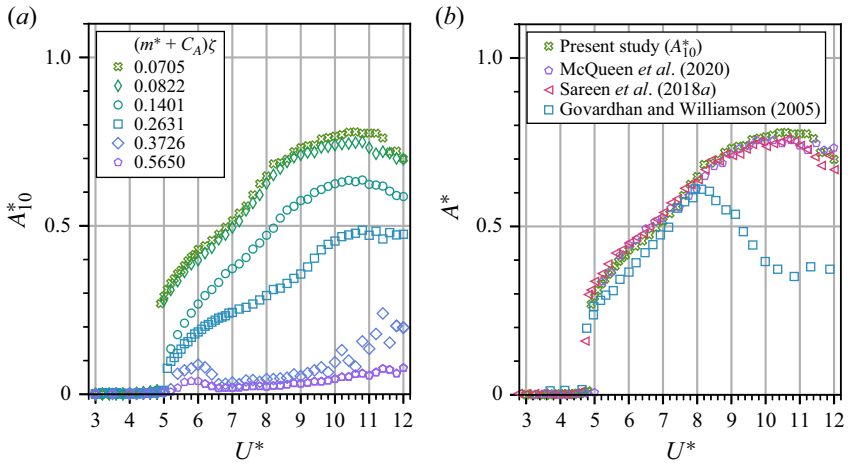


Figure 4. (*a*) Vibration amplitude response (A^*_{10}) as a function of the reduced velocity (U^*) for a sphere ($\epsilon = 1.00$) for various values of the mass-damping parameter $(m^* + C_A)\zeta$. (*b*) Comparison of the vibration response with other studies. The green symbols show the amplitude response (A^*_{10}) for the current study with $m^* = 12.81$ and $(m^* + C_A)\zeta = 0.071$. For the latter cases, the non-dimensional vibration amplitude, $A^* = A/b$, is presented as follows: McQueen *et al.* (2020) with $m^* = 10.1$ and $(m^* + C_A)\zeta = 0.045$; Sareen *et al.* (2018*a*) with $m^* = 14.2$ and $(m^* + C_A)\zeta = 0.059$; Govardhan & Williamson (2005) with $m^* = 31$ and $(m^* + C_A)\zeta = 0.15$.

U^* associated with lock-in remains almost unaffected by an increase in damping ratio. However, there is a slight change in the value of U^* marking the onset of significant FIV from 4.8 and 5.0 over this range. However, the maximum vibration amplitude is strongly affected, changing from $A^*_{10} = 0.76$ for the lowest damped case of $(m^* + C_A)\zeta = 0.0705$ to $A^*_{10} = 0.50$ for $(m^* + C_A)\zeta = 0.2631$. This represents an approximately 34 % decrease. For $(m^* + C_A)\zeta \geqslant 0.3726$, the dynamic response shows the maximum vibration amplitude below 0.1 and is characterised by intermittent bursts of vibration, similar to that reported for a Mode IV of vortex formation by Jauvtis *et al.* (2001), with a difference being the amplitude of oscillation. It should be noted that the increasing trends in A^*_{10} at high reduced velocities (i.e. $U^* > 6.2$) in the cases of $(m^* + C_A)\zeta = 0.3726$ and 0.5650 are associated with aperiodic vibration in desynchronisation, which are similar to the behaviour of tethered spheres shown by Jauvtis *et al.* (2001) and a circular cylinder undergoing inline VIV reported by Zhao *et al.* (2018*b*). Of course, Mode IV was observed to occur at very high U^* values, well beyond the range investigated here. These findings are consistent with previous investigations of FIV of a sphere (e.g. Govardhan & Williamson 2005; Sareen *et al.* 2018*a*). Figure 4(*b*) presents a comparison of the vibration amplitude with other published low-mass-damping responses. Representative data points were extracted from Govardhan & Williamson (2005) for the case $m^* = 31$ and $(m^* + C_A)\zeta = 0.15$, from Sareen *et al.* (2018*a*) for $m^* = 14.2$ and $(m^* + C_A)\zeta = 0.059$, and from McQueen *et al.* (2020) for $m^* = 10.1$ and $(m^* + C_A)\zeta = 0.045$. The amplitude response of the present study shows good agreement with those of Sareen *et al.* (2018*a*) and McQueen *et al.* (2020), both exhibiting a similar amplitude trend and a peak vibration amplitude of approximately 0.75 at $U^* \sim 8$. These cases are for similar mass/mass-damping ratios. The higher mass ratio/mass-damping ratio case of Govardhan & Williamson (2005) shows a lower peak amplitude and reduced response range as would be expected, and indeed is consistent with the higher mass-damped cases shown in figure 4(*a*). Other results from Govardhan & Williamson (2005) for lower masses are consistent with the observed

https://doi.org/10.1017/jfm.2025.10866 Published online by Cambridge University Press

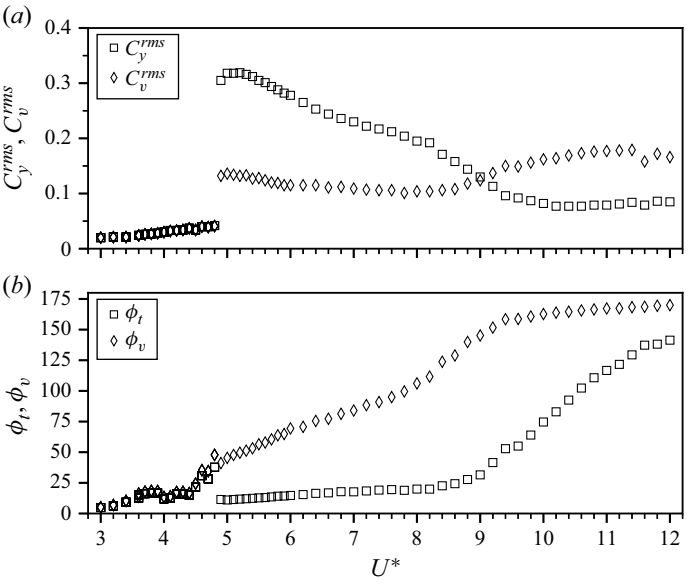


Figure 5. Variation of (*a*) the transverse lift force coefficient (C_y^{rms}) and the vortex force coefficient (C_v^{rms}), and (*b*) the total phase (ϕ_t) and vortex phase (ϕ_v), all as functions of the reduced velocity U^* for a sphere ($\epsilon = 1.00$) with $m^* = 12.81$ and $\zeta = 0.0053$ ($(m^* + C_A)\zeta = 0.0705$) undergoing pure VIV.

response here, but have not been recorded against reduced velocity, preventing a direct comparison.

Figure 5 depicts the variation of the root-mean-square (r.m.s.) values of the total transverse force coefficient, C_y^{rms}, and the vortex force coefficient, C_v^{rms}, along with the total phase, ϕ_t, and vortex phase, ϕ_v, as functions of the reduced velocity, U^*, for $(m^* + C_A)\zeta = 0.0705$. By analysing the variation of the fluid force coefficients and phases, distinct vibration modes related to different vortex formation modes can be identified. As can be seen in figure 5(*a*), a sudden jump in the value of C_y^{rms} from $\sim$0.02 at $U^* = 4.8$ to $\sim$0.3 at $U^* = 4.9$ signifies the onset of the first mode of vibration associated with VIV, referred to as Mode I (M-I) (Govardhan & Williamson 2000; Jauvtis *et al.* 2001). In figure 5(*b*), it can be seen that $\phi_t \sim 10°-25°$ throughout M-I ($4.9 \leqslant U^* \leqslant 9.0$), while ϕ_v progressively increases from $\sim$30° to 150° in the same range U^*. Furthermore, for $U^* \geqslant 9.0$, the total phase rises from 25° and gradually reaches 140°, indicating a transition to the second vibration mode, Mode II (M-II). Again, these findings agree with previous studies on VIV (Govardhan & Williamson 1997, 2000, 2005; Sareen *et al.* 2018*a*; McQueen *et al.* 2020). Both modes in a transversely oscillating sphere ($\epsilon = 1.00$) exhibit hairpin vortex loop structures and counter-rotating streamwise vortex pairs on alternate sides of the wake as the body crosses the centreline (Govardhan & Williamson 2005). The main distinction between these modes lies in the timing of shedding relative to the body motion.

Figure 6 presents the logarithmic scale power spectrum plots, illustrating the dominant oscillation frequency, $f_y^* = f_y/f_{nw}$, content as a function of reduced velocity, U^*. The power spectra were computed using fast Fourier transforms (FFTs) of the displacement time series for each U^* and normalised by the maximum power. As shown in figure 6(*b*), the dominant oscillation frequency remains close to the natural frequency of the system, f_{nw}, throughout the whole vibration range, indicating lock-in. Note that the dashed lines in figure 6(*b*) represent the vortex shedding frequency, f_{vo}^*, of a fixed sphere.

https://doi.org/10.1017/jfm.2025.10866 Published online by Cambridge University Press

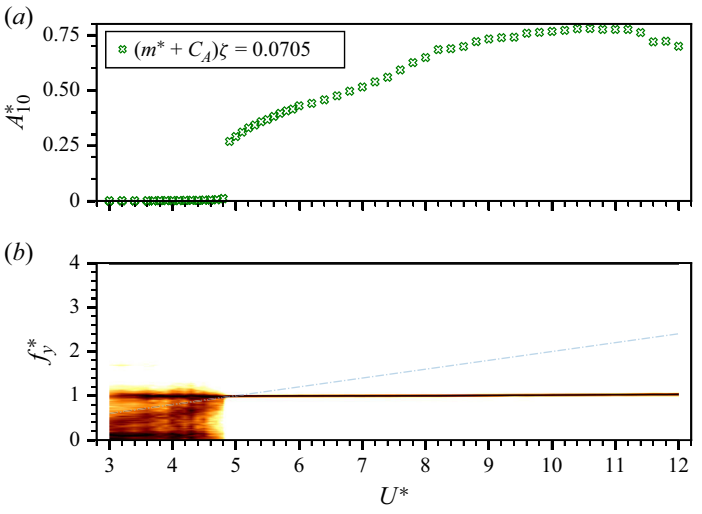


Figure 6. (*a*) Amplitude response and (*b*) logarithmic-scale normalised frequency power spectral density (PSD) contours of the body vibration as a function of the reduced velocity for $\epsilon = 1.00$ with $m^* = 12.81$ and $\zeta = 0.0053$.

3.2. *Effect of the mass-damping parameter on the FIV response of an spheroid of* $\epsilon = 2.00$

The A^*_{10} amplitude response as a function of the reduced velocity (U^*) is plotted in figure 7 for different values of $(m^* + C_A)\zeta$. For low values of the mass-damping parameter ($0.1263 \leqslant (m^* + C_A)\zeta \leqslant 0.7412$), the dynamic response is composed of two distinct FIV phenomena: VIV and a galloping-like response. The VIV region is characterised by the usual inverted-bell shape for A^*_{10} versus U^*, whereas the galloping-like region is characterised by an unbounded linear growth of A^*_{10} beyond a critical value U^*_{crit}. A clear jump in A^*_{10} reveals the transition region between both FIV mechanisms. As the mass-damping parameter is increased to $0.2350 \leqslant (m^* + C_A)\zeta \leqslant 0.3086$, a broad desynchronisation region appears between the end of the VIV region and the onset of the galloping-like region. For mass-damping values in the range $0.3586 \leqslant (m^* + C_A)\zeta \leqslant 0.6171$, the galloping region is entirely suppressed, resulting in a dynamic response comprising only VIV. Finally, for a mass-damping parameter in the range $0.6697 \leqslant (m^* + C_A)\zeta \leqslant 0.7412$, the VIV region is suppressed and the oblate spheroid displays a maximum vibration amplitude $A^*_{10} \leqslant 0.05$ over the entire range of U^* tested.

As the damping ratio value is increased, the U^* range associated with the synchronised VIV response narrows progressively. Figure 8 illustrates the variation of U^*_{jump} (onset of the VIV region) and U^*_{drop} (the end of the VIV region) as a function of $(m^* + C_A)\zeta$. It can be observed that U^*_{jump} values consistently rise from 3.6 to 5.4, while U^*_{drop} values decrease from 9.0 to 6.6, as $(m^* + C_A)\zeta$ is varied from 0.1263 to 0.7412. Over this same range, the magnitude of the peak of the amplitude of vibration, A^*_{10max}, drops from 1.0 to 0.05 as $(m^* + C_A)\zeta$ is increased (see figure 9).

An increment in the mass-damping parameter also impacts the range of U^* associated with the galloping-like regime. Figure 10 illustrates the variation of the critical reduced velocity U^*_{crit} for the onset reduced velocity for a galloping-like response as a function of ζ. For the cases with very low damping of $(m^* + C_A)\zeta \leqslant 0.2012$, the start of the galloping-like response occurs at $U^*_{crit} \sim 9$. A slight increase in the mass-damping value

https://doi.org/10.1017/jfm.2025.10866 Published online by Cambridge University Press

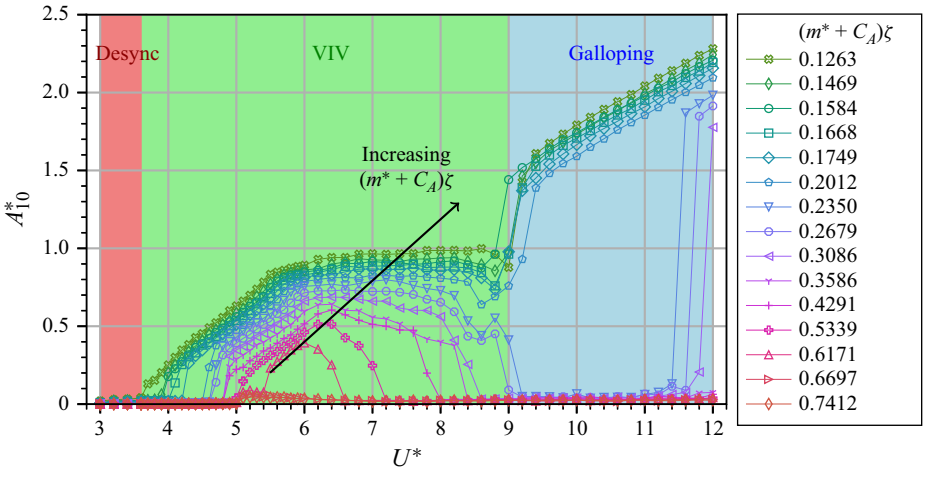


Figure 7. Normalised vibration amplitude response (A^*_{10}) as a function of the reduced velocity (U^*) for an oblate spheroid of $\epsilon = 2.00$ with various values of the mass-damping parameter, $(m^* + C_A)\zeta$.

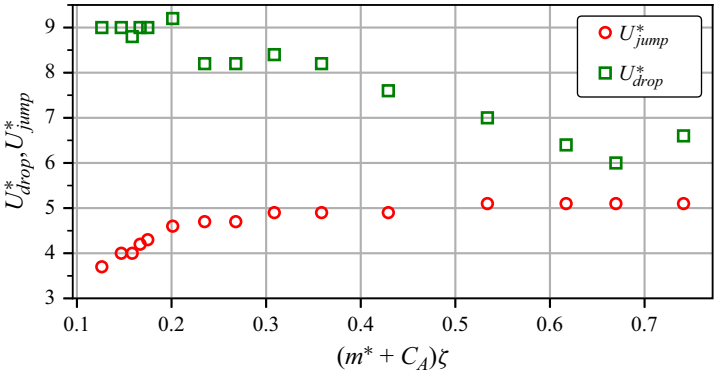


Figure 8. Variation of the reduced velocity indicating the onset of the VIV region, U^*_{jump}, and the reduced velocity associated with the offset, U^*_{drop}, as a function of the mass-damping parameter, $(m^* + C_A)\zeta$ for the $\epsilon = 2.00$ case.

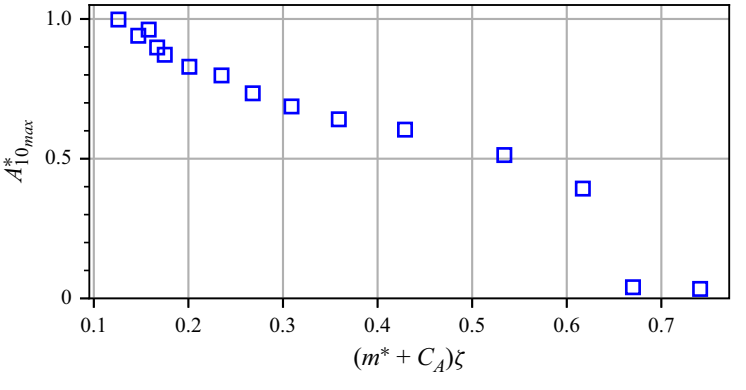


Figure 9. Variation of the maximum amplitude of vibration, $A^*_{10_{max}}$, over the VIV region as a function of the mass-damping parameter, $(m^* + C_A)\zeta$ for the $\epsilon = 2.00$ case.

https://doi.org/10.1017/jfm.2025.10866 Published online by Cambridge University Press

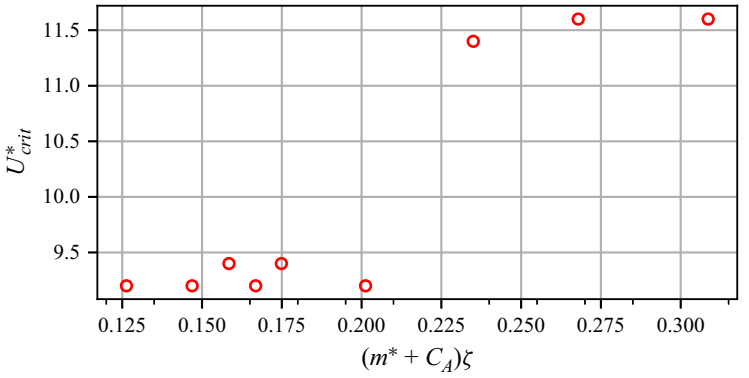


Figure 10. Variation of the critical reduced velocity for the onset of the galloping regime (U^*_{crit}) as a function of the mass-damping parameter, $(m^* + C_A)\zeta$, for $\epsilon = 2.00$. Note that in this case, the range of $(m^* + C_A)\zeta$ is reduced to those cases where galloping is displayed.

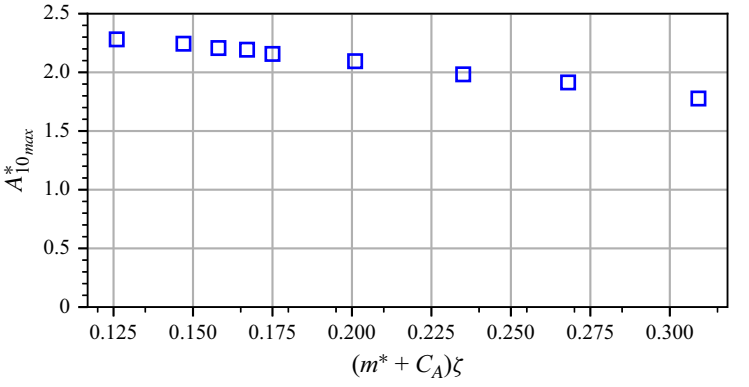


Figure 11. Variation of the maximum amplitude of vibration, $A^*_{10_{max}}$, over the galloping region as a function of the mass-damping parameter, $(m^* + C_A)\zeta$, for $\epsilon = 2.00$.

($(m^* + C_A)\zeta \geqslant 0.2012$) induces a significant shift towards higher values of $U^*_{crit} \geqslant 11.6$, demonstrating that the onset of the galloping-like region is highly sensitive to the value of $(m^* + C_A)\zeta$. Note that the end of the galloping-like region could not be reached for the highest achievable velocities in the water channel due to the capacity of the water pump to deliver higher values of free stream flow velocity (maximum of $450\,\mathrm{mm\,s^{-1}}$) ($\sim U^* = 13.0$). Moreover, there is a noticeable reduction of the maximum amplitude of vibration $A^*_{10_{max}}$ as $(m^* + C_A)\zeta$ is increased. This follows an almost linear decreasing trend, from 2.25 for $(m^* + C_A)\zeta = 0.1263$ to 1.75 for $(m^* + C_A)\zeta = 0.3086$ (see figure 11).

Based on the analysis made by Jauvtis *et al.* (2001), the periodicity of the response can be quantified by defining the periodicity, P, of a signal as

$$P = \sqrt{2} y_{rms}/y_{max}. \tag{3.1}$$

This is equal to unity for a perfectly periodic sinusoidal signal and drops away as the periodicity decreases.

Figure 12 illustrates how the periodicity varies with U^* for various damping ratio values. For example, the case $(m^* + C_A)\zeta = 0.1263$ displays a highly periodic dynamic response

https://doi.org/10.1017/jfm.2025.10866 Published online by Cambridge University Press

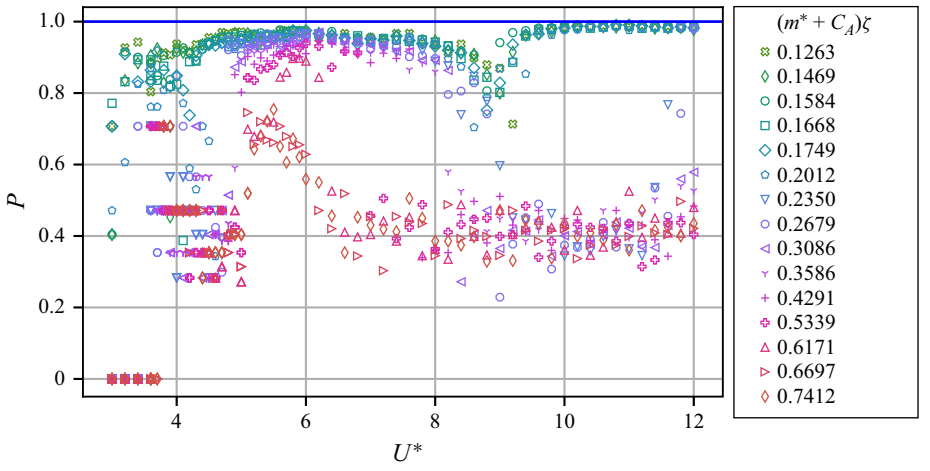


Figure 12. Periodicity of the spheroid displacement as a function of U^* for $\epsilon = 2.00$. The horizontal blue line represents a purely sinusoidal signal.

over both VIV and galloping-like regimes, with a noticeable drop in periodicity during the transition between vibration regimes. This high periodicity of the displacement persists for $(m^* + C_A)\zeta \leqslant 0.2012$ and progressively decreases for the highest values of $(m^* + C_A)\zeta$.

It can be concluded that there are three broad groupings of FIV responses depending on the value of $(m^* + C_A)\zeta$. The first group, labelled Group I, corresponds to values of the mass-damping parameter in the range $0.1263 \leqslant (m^* + C_A)\zeta \leqslant 0.3086$. In this range, the dynamic response is characterised by VIV and galloping-like responses. The second group, labelled Group II, corresponds to the mass-damping parameter in the range $0.3586 \leqslant (m^* + C_A)\zeta \leqslant 0.6171$. In that case, the FIV response consists solely of VIV. As $(m^* + C_A)\zeta$ is increased to $(m^* + C_A)\zeta \geqslant 0.6697$, the vibration amplitude reduces and the synchronisation regions contract, marking a third group, labelled Group III, characterised by a desynchronised response. For the remainder of the study, we will focus on two representative cases to explore more in detail, corresponding to $(m^* + C_A)\zeta = 0.1263$ (representative of Group I) and $(m^* + C_A)\zeta = 0.3586$ (representative of Group II). The actual transition mass-damping parameter value between these groups may be influenced by the reduced velocity range studied since for the low $(m^* + C_A)\zeta$ values from Group I, the response undergoes desynchronisation before establishing a galloping-like response near the upper limit of the U^* range tested.

3.3. *VIV and galloping responses at low mass-damping parameter value (Group I, $\epsilon = 2.00$)*

3.3.1. *Vibration response, fluid forces and phases*

Figure 13 displays the A^*_{10} amplitude response along with the logarithmic-scale power-spectral density (PSD) contour plots of the frequency response of the oblate spheroid oscillation ($f^*_y = f_y/f_{nw}$), the total transverse fluid force ($f^*_{C_y} = f_{C_y}/f_{nw}$) and the vortex force component ($f^*_{C_v} = f_{C_v}/f_{nw}$), as a function of U^* for the lowest mass-damping parameter tested, $(m^* + C_A)\zeta = 0.1263$.

Figure 13(a) reveals that two main vibration regimes can be identified: VIV and galloping-like (vibration). The VIV regime occurs over the range $3.6 \leqslant U^* \leqslant 9.0$ and the galloping-like regime over the range $9.4 \leqslant U^* \leqslant 12.0$.

https://doi.org/10.1017/jfm.2025.10866 Published online by Cambridge University Press

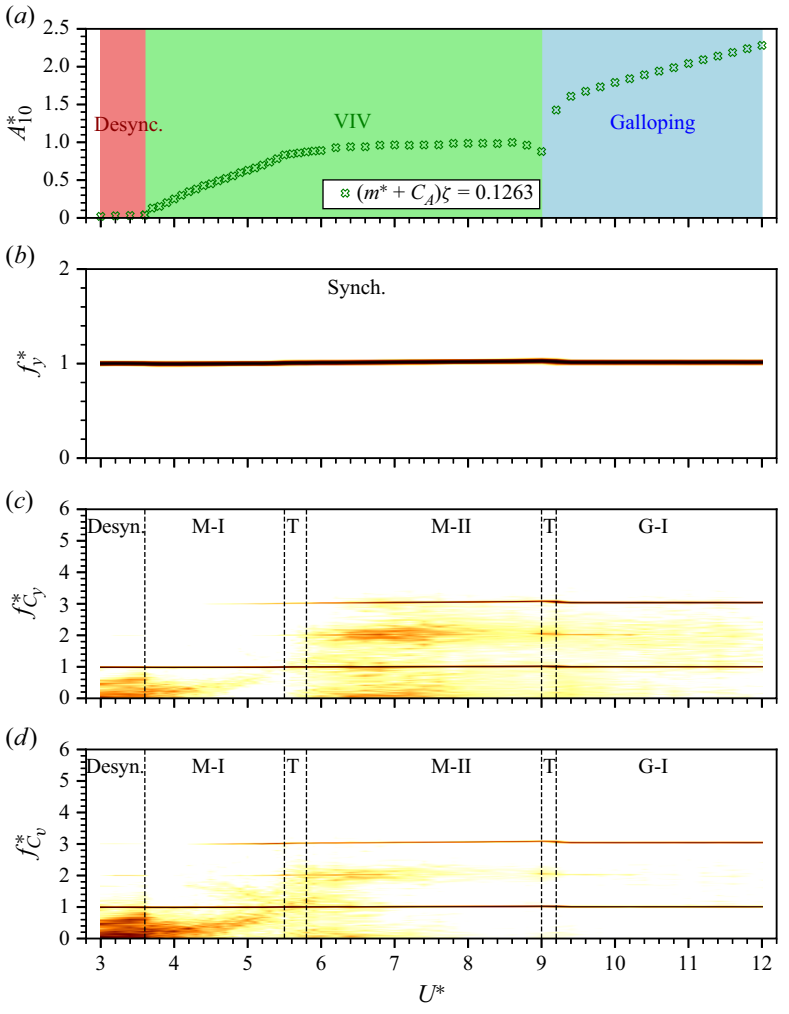


Figure 13. (*a*) Amplitude response and (*b–d*) logarithmic-scale normalised frequency power spectral density (PSD) contours as a function of the reduced velocity for the case of $\epsilon = 2.00$ with $(m^* + C_A)\zeta = 0.1263$. In panels (*b*)–(*d*), vertical dashed lines represent the boundaries of the response regimes. Note the following abbreviations: Mode I (M-I), Mode II (M-II), transition (T) and galloping-like (G-I).

The onset of the VIV regime is marked by a minor jump in the vibration amplitude, from $A^*_{10} \leqslant 0.05$ at $U^* = 3.6$ to $A^*_{10} = 0.15$ at $U^* = 3.7$ (figure 13*a*). The start of the lock-in region is very similar to the case of a non-rotating sphere, where the onset is within the range $4.0 \leqslant U^* \leqslant 5.0$ (see Govardhan & Williamson 2005; Sareen *et al.* 2018*a*). Furthermore, over the range $3.7 \leqslant U^* \leqslant 5.5$, the body vibration frequency (f^*_y), the transverse force frequency ($f^*_{C_y}$) and the vortex force frequency ($f^*_{C_v}$) show a single dominant frequency component close to the natural frequency of the system (f_{nw}) (figure 13*b*,*c*,*d*). This implies the synchronisation between the displacement frequency and the vortex shedding frequency. Thus, the first mode of vortex formation is dominated by VIV, termed Mode I (M-I).

Figure 14 displays the variation of the root-mean-square values of the total transverse force, C_y^{rms}, the vortex force, C_v^{rms}, the total phase (ϕ_t) and vortex phase (ϕ_v) as a function

https://doi.org/10.1017/jfm.2025.10866 Published online by Cambridge University Press

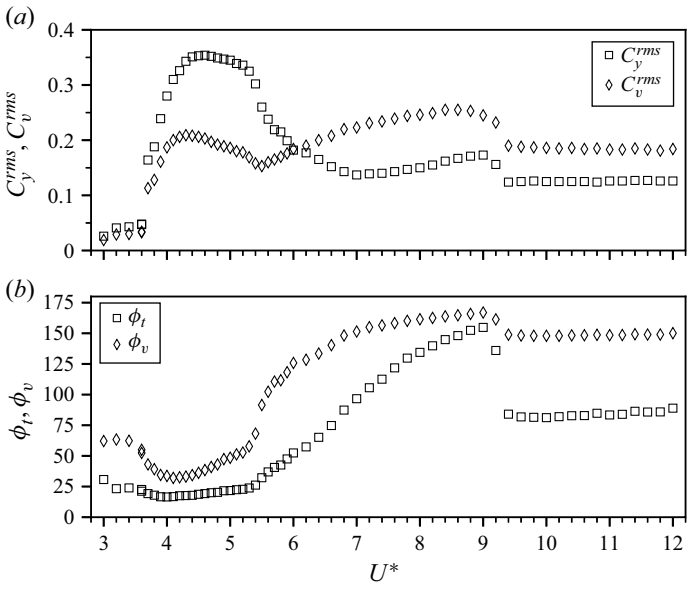


Figure 14. Variation of (*a*) transverse lift force coefficient (C_y^{rms}) and vortex force coefficient (C_v^{rms}), and (*b*) total phase (ϕ_t) and vortex phase (ϕ_v), all as functions of the reduced velocity U^* for $\epsilon = 2.00$ and $(m^* + C_A)\zeta = 0.1263$.

of U^*. The start of M-I is induced by a sudden jump of the fluid force coefficients at $U^* = 3.6$ and then progressively rises until a first magnitude peak is reached. The total phase (ϕ_t) is almost constant at 30° over the range $3.6 \leqslant U^* \leqslant 5.5$, while the vortex phase (ϕ_v) varies slightly between 30° and 50° over the same range. This is similar compared to a non-rotating sphere undergoing VIV, where M-I of VIV is associated with a vortex phase $\phi_v \sim 50°$ (see Govardhan & Williamson 2005; Rajamuni, Thompson & Hourigan 2018; Sareen *et al.* 2018*a*).

With a further increase in the reduced velocity ($U^* \geqslant 5.5$), the vibration amplitude transitions towards a plateau, with A_{10}^* very close to 1.0, marking the appearance of another vortex mode of formation, termed Mode II (M-II) (see figure 13). This mode displays a distinct frequency response compared with M-I; in particular, there is a significant contribution of a superharmonic at three times the body oscillation frequency, $3f_y^*$, in the total transverse and vortex force frequency responses, starting at $U^* = 5.5$. The end of M-II is marked by a noticeable step (i.e. kink) in the frequency responses of $f_{C_y}^*$ and $f_{C_v}^*$ at $3f_y^*$ for the value of $U^* = 9.0$. It is noteworthy that for M-II, the highest significant frequency component is still the one equal to the displacement frequency, f_y^*, suggesting that the FIV responsible for the vibration is associated with VIV.

Figure 14 reveals that the value of C_y^{rms} decreases progressively from its peak 0.35 at $U^* = 5.5$ towards 0.15 at $U^* = 7.0$, indicative of a transition between VIV modes. In addition, there is a second peak displayed by the vortex force coefficient (C_v^{rms}) at $U^* = 8.6$ that marks the peak amplitude of vibration while in M-II. For this mode, ϕ_t grows almost linearly from $\sim 20°$ to 155° in the range $5.5 \leqslant U^* \leqslant 9.0$. Similarly, ϕ_v displays a marked jump at $U^* = 5.5$ and then grows until it reaches a plateau value at 160°. This is consistent with the phase relationship seen for VIV of a sphere, consistent with this oscillation remaining VIV-dominated (see Govardhan & Williamson 2005).

https://doi.org/10.1017/jfm.2025.10866 Published online by Cambridge University Press

For $U^* \geqslant 9.2$, the dynamic response displays a trend similar to a transverse galloping response of a square, D-section or elliptical cylinder (see Zhao *et al.* 2014*b*, 2018*a*; Lo *et al.* 2023), where the amplitude of vibration climbs almost linearly with increasing reduced velocity beyond a critical threshold value, $U^*_{crit} = 9.2$. Over this vibration regime, the amplitude of vibration amplifies from 1.3 at $U^* = 9.2$ to 2.43 at $U^* = 12$, representing an enhancement of 87 % of the amplitude of vibration. Over the range $9.4 \leqslant U^* \leqslant 12.0$, both fluid force components, $f^*_{C_y}$ and $f^*_{C_v}$, reveal strong harmonic contributions at one and three times the displacement frequency (i.e. $f^*_{C_y} = f^*_{C_v} = 1$ and $f^*_{C_y} = f^*_{C_v} = 3$), suggesting that a strong third harmonic contribution can be associated with the high amplitude of vibration. Previous studies of the transverse FIV of bluff bodies (see Zhao *et al.* 2014*b*, 2018*a*,*c*; Wang *et al.* 2017) or in-line FIV (see Bourguet & Lo Jacono 2015; Zhao *et al.* 2018*b*) suggested that large-amplitude vibrations are attributable to harmonic synchronisation. For the spheroid case, the wake-body synchronisation involves the vortex and total transverse force harmonics, which leads to a galloping-like oscillation response termed Mode G–I.

Figure 14 shows that a sharp drop in ϕ_t, from 150° at $U^* = 9.0$ to 90° at $U^* = 9.4$, characterises the transition between VIV and galloping-like. Beyond that, ϕ_t and ϕ_v remain almost linear at 90° and 145°, respectively. Similarly, for Mode G-I, both fluid force coefficients, ${C_y}^{rms}$ and ${C_v}^{rms}$, remain nearly constant at 0.13 and 0.18, respectively, over the entire range $9.2 \leqslant U^* \leqslant 12.0$.

3.3.2. *Wake modes*

In this subsection, PIV measurements are analysed to characterise the wake modes in terms of their vorticity patterns.

Figure 15 illustrates phase-averaged PIV snapshots for Mode I for a sequence of increasing reduced velocities: $U^* \in [4.5, 5.0, 5.5]$. Four phase-averaged PIV snapshots (selected from 48 phases) are presented in the columns. The images are structured as follows: the first column from left to right shows the wake dynamics of the oblate spheroid at the equilibrium position, the second column corresponds to the oblate spheroid at the highest displacement point, the third column is associated with another equilibrium position and the fourth column displays the wake structure at the lowest position. Due to the 3-D and turbulent nature of the flow at high Reynolds numbers, the wake vortex shedding is complex; however, several phase-average coherent structures can be discerned in the laser plane, and the average flow dynamics can be inferred from the visualisations. In this study, the nomenclature for the wake patterns is based on the terminology introduced by Williamson & Roshko (1988). Note that the interpretations supplied here result from viewing the wake animations; these interpretations are more difficult to arrive at from the presented sets of still images in the figures. The movie images are included in the supplementary material to help the reader understand the wake structure formation for the oscillating oblate spheroid.

As illustrated in figure 15, the low-damped case of $(m^* + C_A)\zeta = 0.1263$ in the M-I regime exhibits a $2(P + S)$ wake mode, characterised by two pairs of counter-rotating vortices (P) along with two single vortices (S) of opposite-sign shed per body oscillation cycle. For $U^* = 4.50$, when the body moves upwards towards its top position, the wake is deflected in the opposite direction (i.e. downwards), composed of a pair of counter-rotating vortices P_1, and a single vortex of negative vorticity S_1; similarly, when the oblate spheroid moves towards its lowest position, the wake is deflected upwards, displaying another pair of counter-rotating vortices P_2 along with a single vortex S_2. The wake shows the half-period flip symmetry, similar to that of an oscillating sphere or cylinder experiencing VIV (see Blackburn, Marques & Lopez 2005; Rajamuni *et al.* 2018; Sareen *et al.* 2018*a*;

https://doi.org/10.1017/jfm.2025.10866 Published online by Cambridge University Press

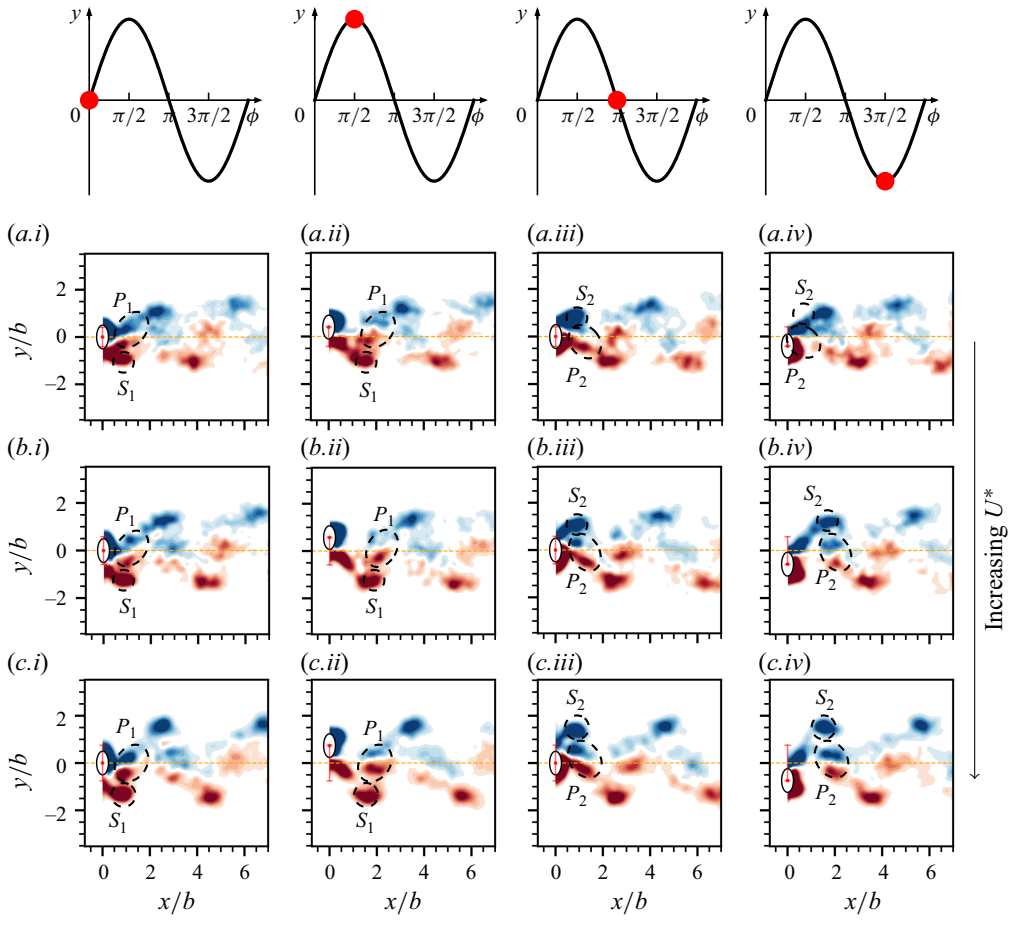


Figure 15. Wake patterns visualised from PIV spot measurements in the Mode-I regime for $\epsilon = 2.00$ and $(m^* + C_A)\zeta = 0.1263$ at (a) $U^* = 4.5$, (b) $U^* = 5.0$, and (c) $U^* = 5.5$. The normalised vorticity range is $\omega^* = \omega b/U \in [-3, 3]$, with ω being the vorticity. The horizontal dashed line at $y/b = 0$ denotes the centreline of the zero flow condition, facilitating a clearer observation of the wake deflection. At the same time, the vertical red bar located at x/b signifies the vibration ranges. The fluid flow in the images is from left to right. The blue is for negative vorticity and the red is for positive vorticity. The red point (·) on the sine waves shows the corresponding position of the spheroid during the oscillation cycle. Note that the oscillations during the synchronised regimes shown here are assumed to be sinusoidal; thus, the sinusoid symbolically represents the displacement of the oblate spheroid. Supplementary movies are included available at https://doi.org/10.1017/jfm.2025.866 to help the reader understand the wake structure formation for the oscillating oblate spheroid.

Eshbal *et al.* 2019*b*; Mishra, Bhardwaj & Thompson 2024). As the reduced velocity is increased to $U^* = 5.5$, the detachment of the shear layer occurs closer to the afterbody; however, the deflection angle of the wake appears similar.

Figure 16 exhibits sample time traces of the fluid forces and the spheroid displacement as a function of the dimensionless time $\tau = t/T_{nw} = tf_{nw}$, alongside the power spectral density (PSD) of these signals as a function of the dimensionless frequency, $f^* = f/f_{nw}$, for the corresponding U^* displayed in figure 15. Figure 16 shows that both the total transverse force (C_y) and the vortex force (C_v) are generally in phase with the body displacement (y^*) over the range of velocities associated with M-I. This agrees with the

https://doi.org/10.1017/jfm.2025.10866 Published online by Cambridge University Press

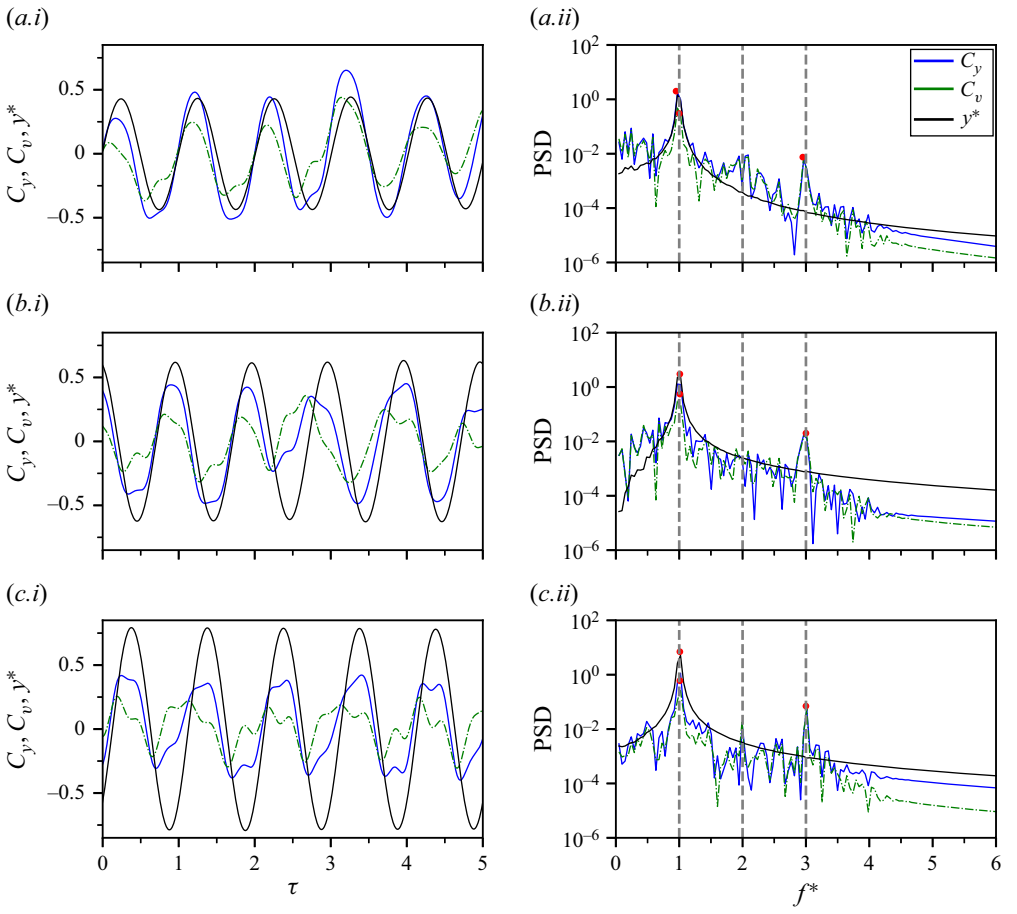


Figure 16. Sample time traces of the body displacement (y^*), and the coefficients of the total transverse force (C_y) and the vortex force (C_v) within the M-I regime, along with the corresponding frequency PSD plots for $\epsilon = 2.00$ and $(m^* + C_A)\zeta = 0.1263$ at (*a*) $U^* = 4.5$, (*b*) $U^* = 5.0$, and (*c*) $U^* = 5.5$. The time traces are plotted as a function of the dimensionless time $\tau = tf_{nw}$ and the power spectrum as a function of f^*. The red dots (•) in the power spectrum highlight multiple harmonic contributions.

results presented in figure 14 where both fluid force phases are below 90°. The PSD plots reveal that the most powerful frequency contribution is attributed to $f^* = 1$.

As shown in figure 17, for M-II, the oblate spheroid wake depicts a $2(P + S)$ structure, similar to the one exhibited in M-I. For example, figure 17(*c*) displays the wake structure of the vortex shedding at $U^* = 8.0$. The wake deflection angle increases along with a more elongated shear layer and stronger interaction between opposite-signed shear layers relative to M-I as shown in figure 15. As the spheroid ascends, it sheds a single vortex, S_1, followed by a pair of counter-rotating vortices, P_1. Conversely, when the spheroid descends, another single vortex, S_2, is shed before a pair of counter-rotating vortices, P_2. The primary difference from M-I lies in the deflection angle of the wake and the timing of the formation of the vortical structures.

Figure 18 demonstrates that both fluid force coefficients (i.e. the total transverse and vortex forces) are evidently out of phase with respect to the body displacement. This is in contrast to the M-I case shown in figure 16. The PSD plots indicate the presence of two peaks associated with the frequency harmonic components of $f^* = 1$

https://doi.org/10.1017/jfm.2025.10866 Published online by Cambridge University Press

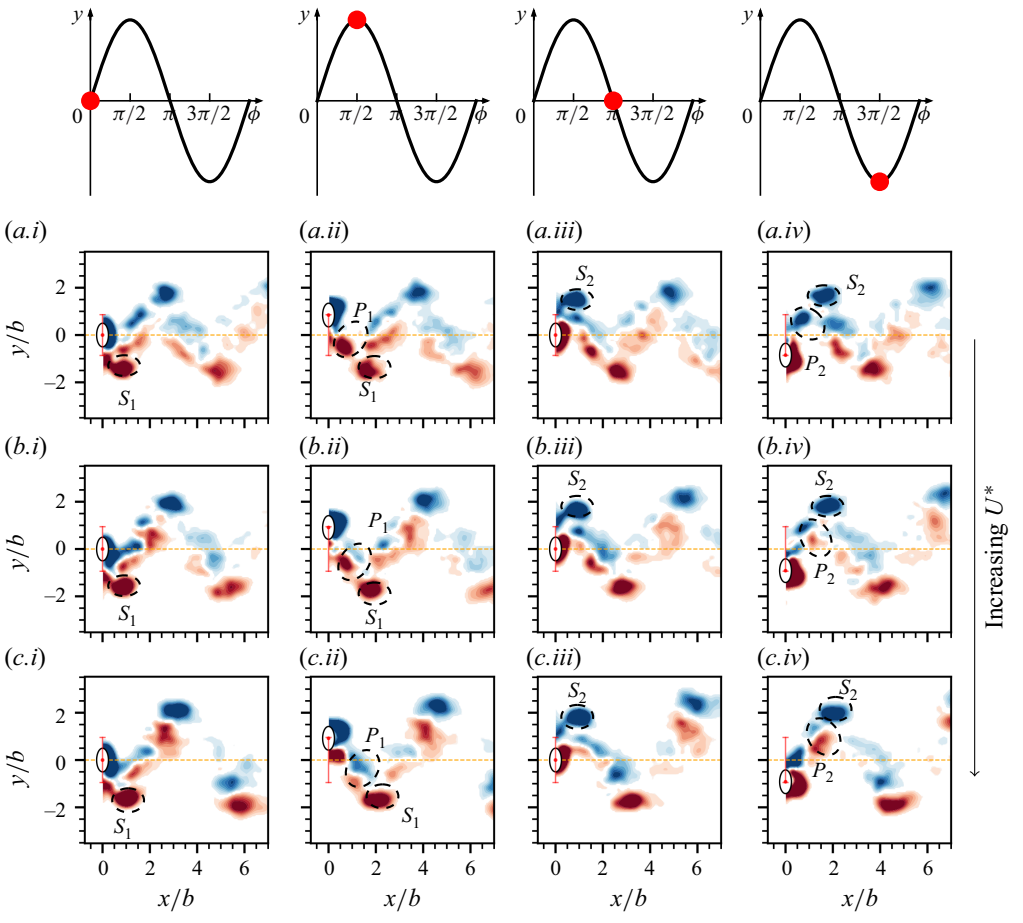


Figure 17. Wake patterns visualised from PIV spot measurements in the M-II regime for $\epsilon = 2.00$ and $(m^* + C_A)\zeta = 0.1263$ at (*a*) $U^* = 6.0$, (*b*) $U^* = 7.0$ and (*c*) $U^* = 8.0$. The red point on the sine waves shows the corresponding position of the spheroid within the oscillation cycle. The movie images are included in the supplementary material to help the reader understand the wake structure formation for the oscillating oblate spheroid.

and $f^* = 3$, characterised by an approximately equal power contribution for this vibration regime.

Figure 19 reveals the sample PIV vorticity fields of the galloping-like regime G-I for $U^* \in [10.0, 11.0, 12.0]$. The wake pattern associated with this vibration regime is $2(3P + S)$, characterised by four pairs of opposite-sign vortices (P) and two single vortices of opposite vorticity (S) shed per body oscillation cycle. Compared with the wake structure displayed in M-I and M-II, there is a significant enlargement (i.e. longer) of the shear layers combined with larger body vibrations. Furthermore, there is a stronger interaction between opposite-signed shear layers, resulting in a higher number of vortical structures shed per oscillation cycle compared with VIV modes. The number of distinct vortex structures per cycle may increase for higher values of the reduced velocity, although this was not tested.

Figure 20 exhibits the sample time traces of the structural (body displacement) and fluid (transverse and vortex force) dynamics corresponding to the PIV visualisation shown in figure 19. For Mode G-I, both C_y and C_v display two dominant frequencies that

https://doi.org/10.1017/jfm.2025.10866 Published online by Cambridge University Press

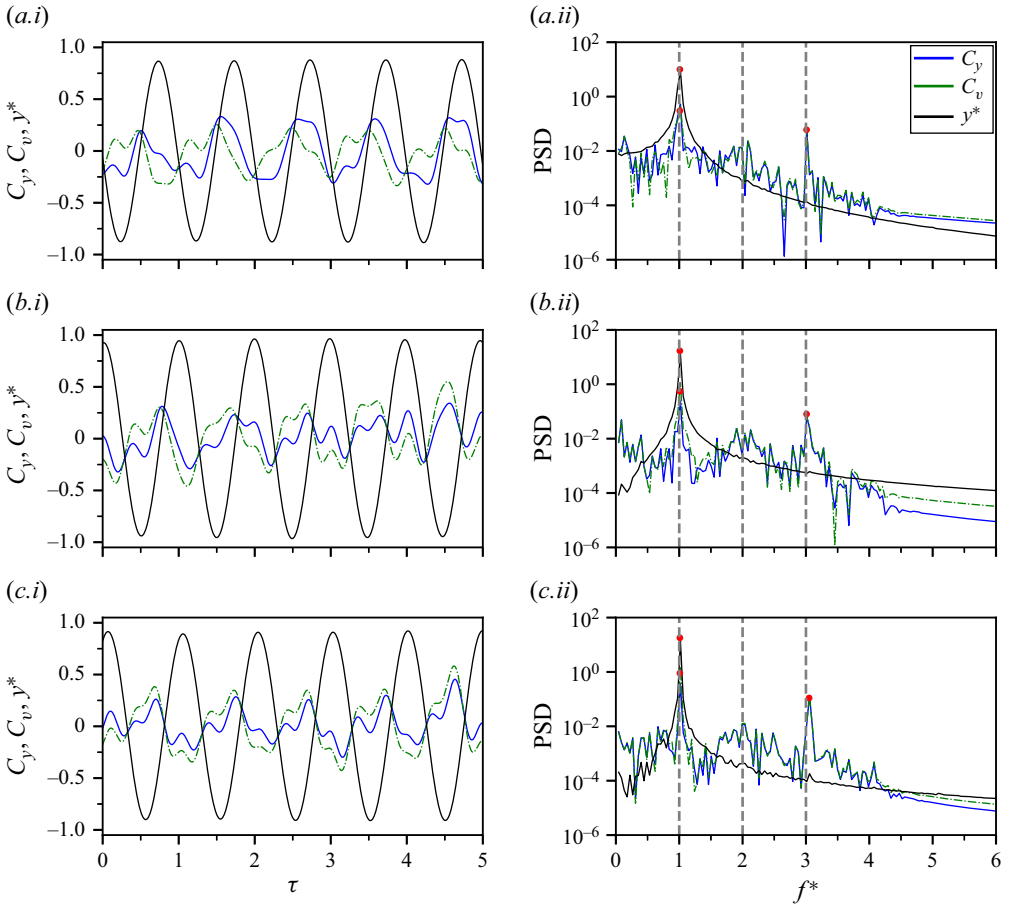


Figure 18. Sample time traces of the body displacement (y^*), and the coefficients of the total transverse force (C_y) and the vortex force (C_v) within the M-II regime, along with the corresponding frequency PSD plots for $\epsilon = 2.00$ and $(m^* + C_A)\zeta = 0.1263$ at (*a*) $U^* = 6.0$, (*b*) $U^* = 7.0$ and (*c*) $U^* = 8.0$. The red dots (●) in the power spectrum highlight multiple harmonic contributions.

have approximately equal power contributions, matching the body vibration frequency at $f^* = 1$ and a harmonic at $f^* = 3$. In this case, the total phase remains close to 90°, suggesting that the transverse total force is nearly in phase with the body's velocity; therefore, supporting the body vibration and inducing a galloping-dominated response.

It is noteworthy that the second harmonic in the fluid forcing ($f^*_{C_y}$ and $f^*_{C_v}$) seems to correlate with the number of vortex pairs (i.e. the number of '*P*') in the wake pattern. For instance, a relatively weak second harmonic is observed in the $2(P + S)$ patterns in M-I and M-II. However, as demonstrated by Cordero Obando *et al.* (2024), in the $2(2P + S)$ pattern observed in the V-II regime for $\epsilon = 3.20$, the second harmonic of $f^*_{C_y}$ exceeds the third harmonics in strength. Conversely, in the $2(3P + S)$ mode during the G-I regime of $\epsilon = 2.00$ in the present study, the third harmonic appears to be second-strongest frequency component, while the second harmonic becomes negligible (see figure 20).

https://doi.org/10.1017/jfm.2025.10866 Published online by Cambridge University Press

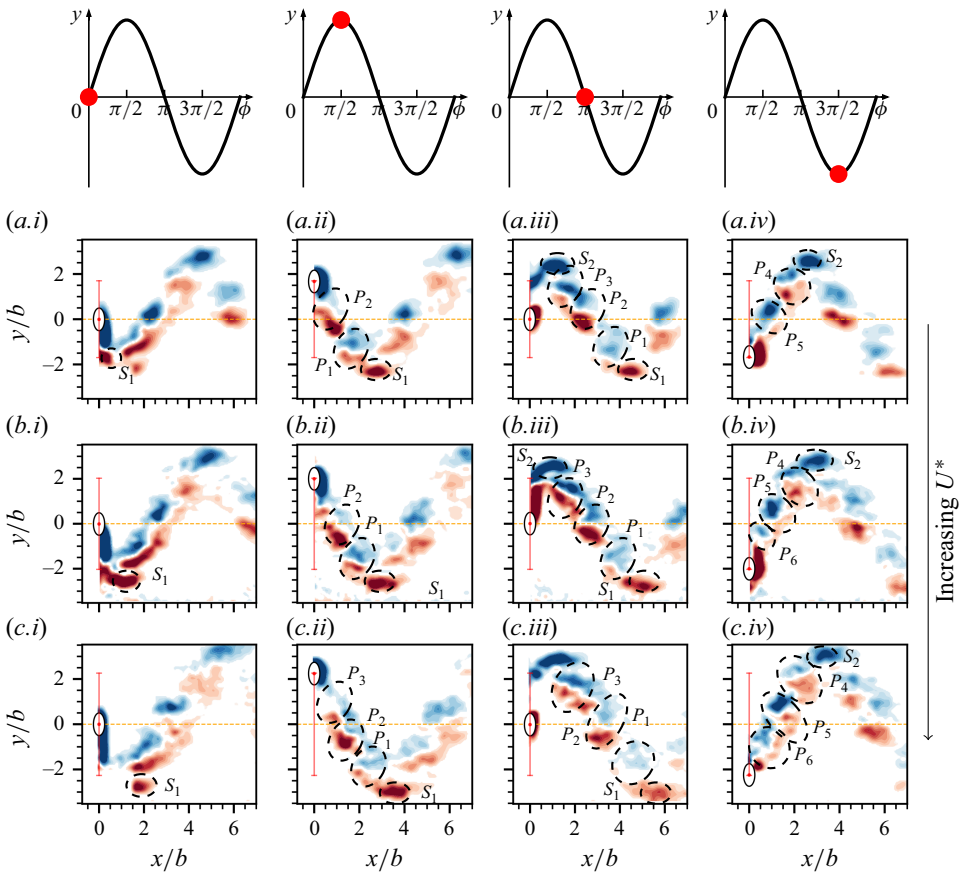


Figure 19. Wake patterns visualised from PIV spot measurements within the G-I regime for $\epsilon = 2.00$ and $\zeta = 0.0050$ at (*a*) $U^* = 10.0$, (*b*) $U^* = 11.0$ and (*c*) $U^* = 12.0$. The red point on the sine waves shows the corresponding position of the spheroid during the oscillation cycle. The movie images are included in the supplementary material to help the reader understand the wake structure formation for the oscillating oblate spheroid.

3.4. *Analysis of galloping response*

MIE occurs naturally when a body moves through a fluid and ceases when the body comes to rest. As the body accelerates, the resulting unsteady flow alters the fluid forces acting on it. If these changes produce negative damping or facilitate energy transfer to the body, self-excited vibrations may arise, a phenomenon defined as MIE.

3.4.1. *Quasi-steady analysis*

This section examines the potential for galloping through a quasi-steady analysis, focusing on the lift force (F_L), drag force (F_D) and transverse force (F_y) acting on a static body as the angle of incidence, α, changes. The approach assumes that the different phases of vibration are quasi-steady, meaning there is little to no phase difference between the fluid forces and the body's velocity. Under this assumption, the instantaneous excitation force acting on the moving structure is closely approximated by the static force at the corresponding instantaneous angle of attack (Naudascher & Rockwell 2005).

For an elastically mounted bluff body undergoing FIV with a transverse velocity, $\dot{y}$, the relative velocity between the moving body and the free stream flow has a magnitude, $U_{rel} = \sqrt{U + \dot{y}^2}$, and an angle, $\tan(\alpha') = \dot{y}/U$ (figure 21).

https://doi.org/10.1017/jfm.2025.10866 Published online by Cambridge University Press

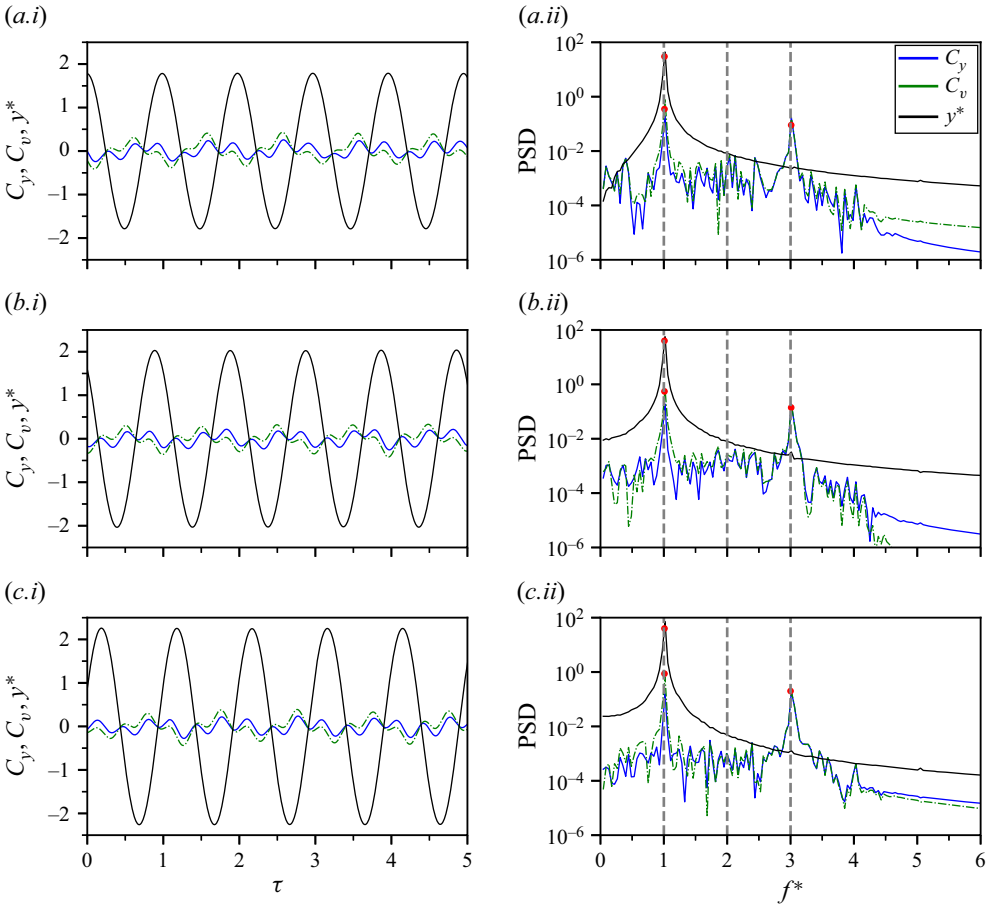


Figure 20. Sample time traces of the body displacement (y^*), and the coefficients of the total transverse force (C_y) and the vortex force (C_v) within the G-I regime, along with the corresponding frequency PSD plots for $\epsilon = 2.00$ and $(m^* + C_A)\zeta = 0.1263$ at (*a*) $U^* = 10.0$, (*b*) $U^* = 11.0$ and (*c*) $U^* = 12.0$.

Figure 22 displays the variations of the mean quasi-steady coefficients of the lift ($C_{L,q}$), and drag ($C_{D,q}$) as a function of inclination angle of attack in the range of $-10° \leqslant \alpha \leqslant 90°$ at different fixed Reynolds numbers in the range $7500 \leqslant Re \leqslant 19\,840$. It can be seen that the drag coefficient ($C_{D,q}$) attains a maximum value of 0.85 at an incidence angle of $\alpha = 0°$, progressively decreasing to a global minimum of 0.25 at $\alpha = 90°$. Notably, the drag coefficient variation seems to follow a common trend independent of the Reynolds number value within the tested range. However, the lift coefficient ($C_{L,q}$) starts at 0 for $\alpha = 0°$ and reaches an absolute value of 0.42 at $\alpha = 58°$. Within this range of inclination angle, the trend followed by $C_{L,q}$ seems to be uncorrelated with the value of Re. Furthermore, beyond $\alpha \geqslant 58°$, there is an inflexion point for $Re \geqslant 15\,000$, marked by a sudden jump in the magnitude of $C_{L,q}$ from 0.42 to 0.67 between 58° and 59°, and then a decrease in the magnitude of $C_{L,q}$ until reaching 0 at $\alpha = 90°$. This change in the shape of $C_{L,q}$ denotes a change in the regime flow, most likely associated with a change in the wake structure.

When compared with figure 23 for the oscillating case, it can be seen that the range of U^* associated with a galloping-like response displays an almost constant value of maximum relative angle of attack (α'_{max}) between 45° and 50°, a value that is close to

https://doi.org/10.1017/jfm.2025.10866 Published online by Cambridge University Press

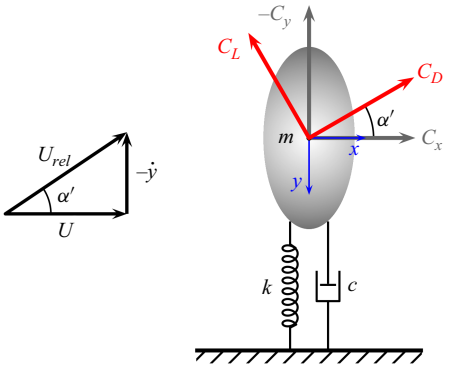


Figure 21. Sketch of the relative velocity and fluid forces experienced by an oblate spheroid moving transversely in a free stream flow. Note that $\dot{y}$ is the body's velocity, U_{rel} is the relative velocity and α' is the relative (effective) angle of attack; C_L and C_D are the lift and drag coefficients with respect to U_{rel}, respectively, while C_y and C_x are the transverse and streamwise force coefficients, respectively.

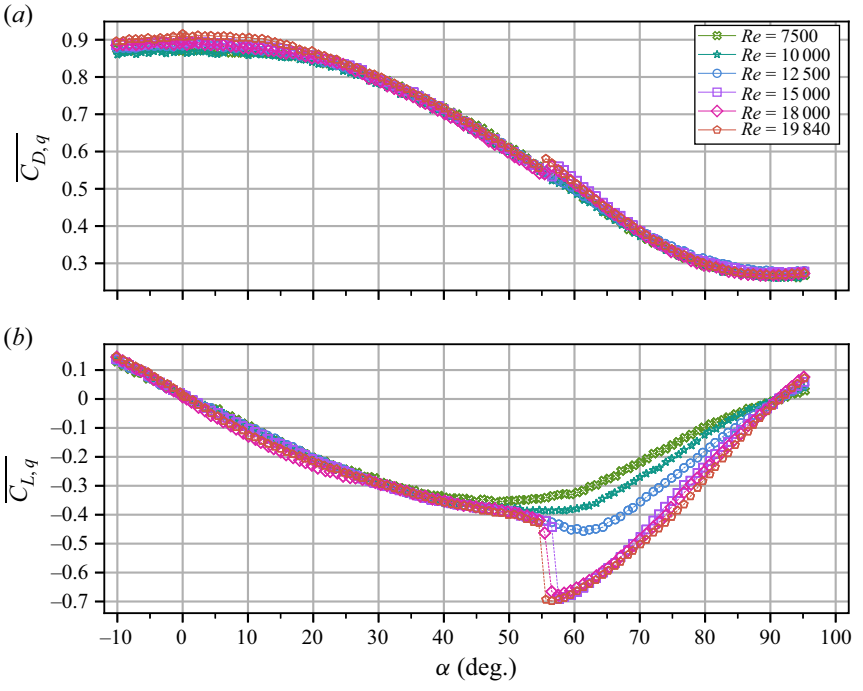


Figure 22. (*a*) $C_{L,q}$ and (*b*) $C_{D,q}$, which are the lift and drag coefficients, respectively, obtained from static tests as a function of the inclination angle α for the $\epsilon = 2.00$ spheroid at various Reynolds numbers.

that associated with the inflexion point for the static case. Note that the instantaneous relative angle of attack is calculated as $\alpha'(t) = \tan^{-1}(\dot{y}(t)/U)$.

To assess if the oblate spheroid with an aspect ratio of $\epsilon = 2.00$ is susceptible to galloping oscillations under soft excitation (i.e. small-amplitude excitation from rest), a stability criterion can be derived from the following equation of motion:

$$m\ddot{y} + 2m\zeta\omega_n\dot{y} + m{\omega_n}^2 y = \frac{\pi}{8}\rho U^2 b^2 C_y, \tag{3.2}$$

https://doi.org/10.1017/jfm.2025.10866 Published online by Cambridge University Press

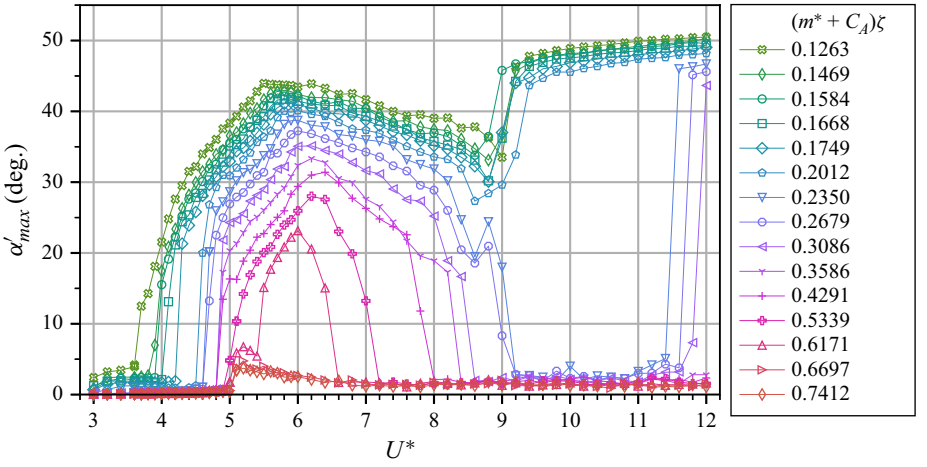


Figure 23. Variation of the maximum relative angle of attack, α'_{max}, as a function of the reduced velocity, U^*, for $\epsilon = 2.00$ with various values of $(m^* + C_A)\zeta$.

where $\omega_n = 2\pi f_{nw}$ is the natural angular frequency of the system. Based on the quasi-steady theory by Parkinson & Smith (1964), the transverse fluid force coefficient (C_y) for small amplitude excitation can be approximated as a first-degree polynomial (Naudascher & Rockwell 2005):

$$C_y = a_1 \frac{\dot{y}}{U}. \tag{3.3}$$

Substituting (3.3) in (3.2) yields

$$\ddot{y} + \left(\frac{2\zeta\omega_n}{m} - \frac{\pi\rho U b^2}{8m} a_1 \right) \dot{y} + \omega_n^2 y = 0. \tag{3.4}$$

According to (3.4), the dynamical system becomes unstable if the combined damping term (i.e. the sum of structural and aerodynamic damping) is negative:

$$\frac{2\zeta\omega_n}{m} - \frac{\pi\rho U b^2}{8m} a_1 < 0. \tag{3.5}$$

Here, the sign of the damping term is determined solely by a_1, as all other quantities are positive. Transverse galloping from rest occurs if $a_1 = \beta_{qs} = \partial C_y/\partial\alpha = -(\partial C_{L,q}/\partial\alpha + C_{D,q}) \geqslant 0$, a condition known as the Den Hartog criterion (Naudascher & Rockwell 2005). It is noteworthy that a_1 represents the slope of the transverse force coefficient (C_y) at zero angle of attack, $\alpha = 0°$. Based on the Den Hartog criterion, the oblate spheroid does not exhibit galloping from rest, as $a_1 < 0$. Specifically, at $\alpha = 0°$, a_1 has a value of -0.1 (see figure 24). The lift and the drag forces contribute to damping, confirming that the oblate spheroid is not susceptible to soft galloping.

It is also insightful to consider the potential for the oblate spheroid to exhibit hard galloping, defined as the onset of vibration triggered by a finite-amplitude disturbance (Novak 1972). For this analysis, an expression for the quasi-steady transverse force coefficient ($C_{y,q}$) is required as a function of the measured quasi-steady lift ($C_{L,q}$) and quasi-steady drag ($C_{D,q}$):

$$C_{y,q}(\alpha) = -\frac{1}{\cos(\alpha)} \left(C_{L,q} + C_{D,q} \tan(\alpha) \right). \tag{3.6}$$

https://doi.org/10.1017/jfm.2025.10866 Published online by Cambridge University Press

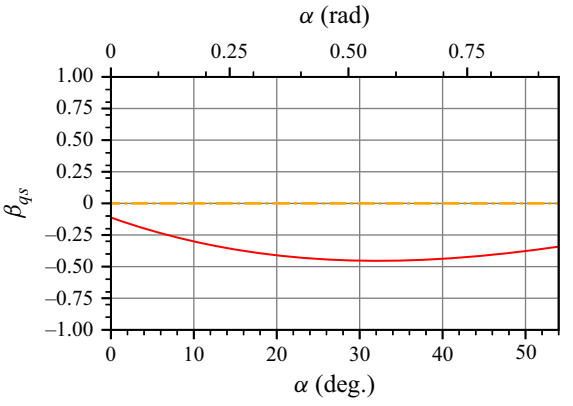


Figure 24. Variation of the quasi-steady stability criteria β_{qs} computed from the quasi-steady force coefficients as a function of the incidence angle of attack, α.

A key factor to consider is the instantaneous quasi-steady power coefficient, $C_{p,q}$, which represents the energy transfer from the fluid to the oblate spheroid due to the transverse force. If $C_{p,q} > 0$, the transverse force amplifies the vibration of the structure, while negative values indicate that any vibration due to the transverse force will be damped. The power coefficient was computed as follows:

$$C_{p,q}(\alpha) = C_{y,q}\dot{y} = U\tan(\alpha)C_{y,q}. \tag{3.7}$$

Figure 25 shows the variation of the quasi-steady lift ($C_{L,q}$), drag ($C_{D,q}$), transverse ($C_{y,q}$) and power ($C_{p,q}$) coefficients against the inclination angle of attack, α, at a Reynolds number of $Re = 19\,800$. According to (3.6), the lift contributes positively to the transverse force, while the drag opposes the motion. For all the angles of attack tested ($0° \leqslant \alpha \leqslant 55°$), the lift ($C_{L,q}$) remains negative in the range ($-0.4 \leqslant C_{L,q} \leqslant 0.4$), while the drag ($C_{D,q}$) remains positive in the range ($0.5 \leqslant C_{D,q} \leqslant 0.9$). For all the values of α, the drag dominates the lift in (3.6) (see figure 25*c*), generating a negative power contribution (see figure 25*d*), therefore attenuating the motion. Thus, based on this quasi-steady analysis, no energy from the flowing fluid is added to the structure. Consequently, based on quasi-steady analysis, the oblate spheroid is not susceptible to developing hard galloping either.

3.4.2. *Instantaneous force coefficients*

This subsection presents the force and power coefficients derived from the FIV experiments and contrasts them with the quasi-steady predictions outlined in § 3.4.1. Figure 26 presents the variation of the instantaneous fluid force and power coefficients as a function of the relative angle of attack, α', for different values of reduced velocity $U^* = 6, 7, 8, 9, 10, 11$ and 12. These values of U^* are associated with different dynamic response regimes. The lift (C_L) and drag (C_D) coefficients were computed as a function of the relative angle of attack (α'), and the transverse (C_y) and streamwise (C_x) coefficients:

$$C_L(\alpha') = \frac{C_y\cos(\alpha') - C_x\sin(\alpha')}{1+\tan^2(\alpha')} \tag{3.8}$$

$$C_D(\alpha') = \frac{C_y\sin(\alpha') + C_x\cos(\alpha')}{1+\tan^2(\alpha')}. \tag{3.9}$$

https://doi.org/10.1017/jfm.2025.10866 Published online by Cambridge University Press

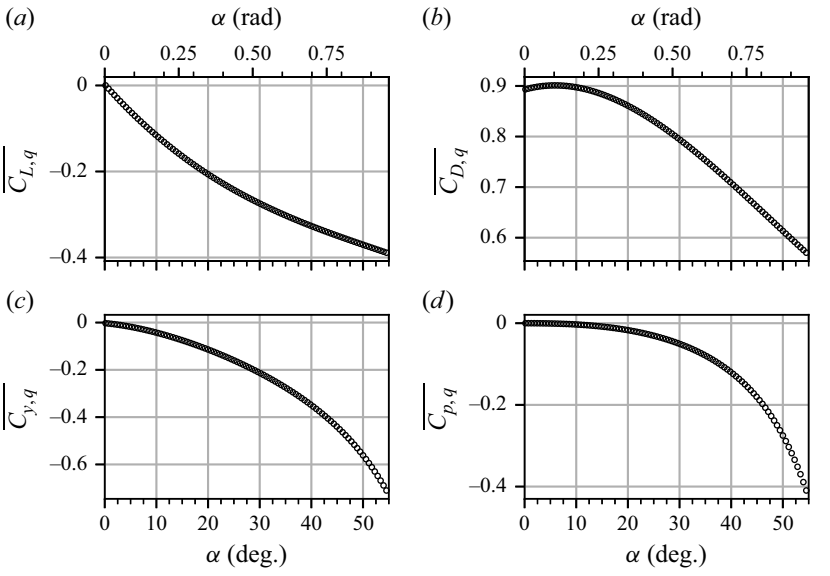


Figure 25. Variation of the (*a*) lift $C_{L,q}$, (*b*) drag $C_{D,q}$, (*c*) transverse $C_{y,q}$ and (*d*) power $C_{p,q}$ coefficients as a function of the inclination angle α for the quasi-steady model, obtained from force measurements on the fixed spheroid of $\epsilon = 2.00$ for a Reynolds number of $Re = 19\,840$.

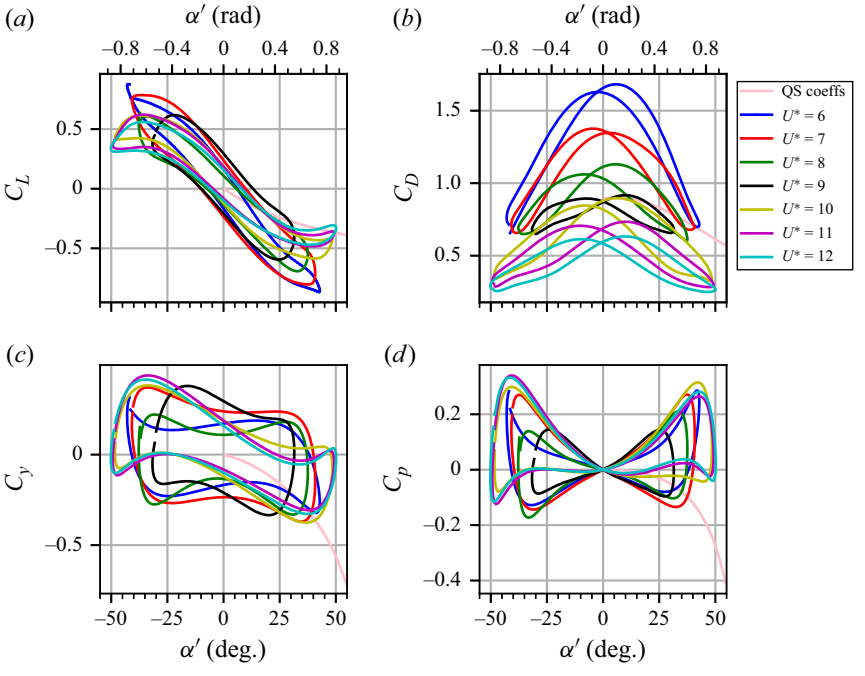


Figure 26. Variation of the instantaneous (*a*) lift (C_L), (*b*) drag (C_D), (*c*) transverse force (C_y) and (*d*) power coefficients (C_p) obtained from an elastically mounted oblate spheroid oscillating as a function of the relative angle of attack (α') at different values of U^*. Note that the quasi-steady force coefficients for $Re = 19\,840$ are plotted to compare both approaches.

https://doi.org/10.1017/jfm.2025.10866 Published online by Cambridge University Press

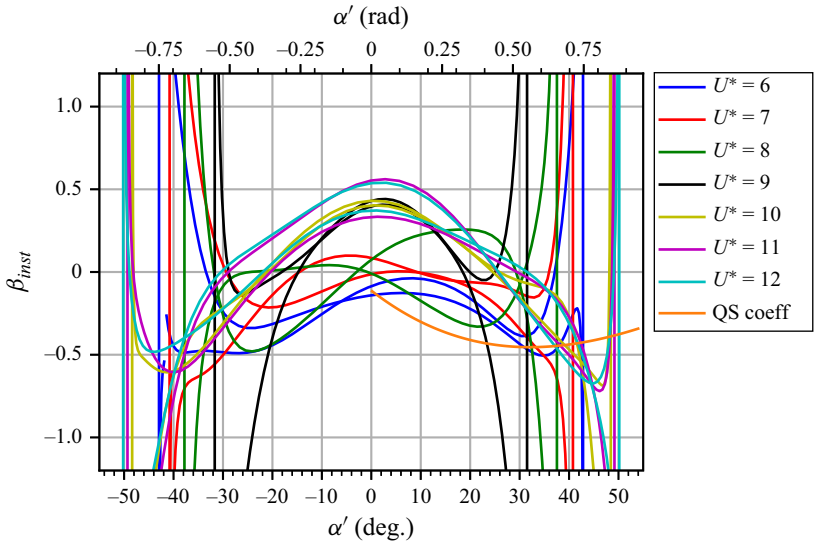


Figure 27. Variation of the instantaneous stability criteria β_{inst} computed from the instantaneous force coefficients as a function of the relative angle of attack, α'. Note that the variation of the quasi-steady stability criteria (β_{qs}) is included along with the instantaneous values of the stability criteria (β_{inst}).

First, it is evident that the instantaneous lift coefficient (C_L) exhibits a general trend across all values of U^*, ranging approximately in the range $-0.6 \leqslant C_L \leqslant 0.6$. Compared with the quasi-steady lift ($C_{L,q}$), both show good agreement, indicating that the lift variations are primarily due to quasi-steady effects and are relatively insensitive to changes in Reynolds number. Conversely, the instantaneous drag coefficient (C_D) is influenced by U^* (i.e. Reynolds number), leading to significant variations depending on the dynamic response regime. Compared with the quasi-steady drag ($C_{D,q}$), there is a noticeable difference between their values depending on the dynamic response regime in which the instantaneous force measurement is taken. This suggests that in addition to a quasi-steady effect, there is a vortex-shedding effect that modifies the behaviour of the drag. Regarding energy transfer, certain values of the relative angle of attack exhibit a positive energy contribution (see figure 26*d*). This enhances the oblate spheroid motion and sustains large amplitude vibrations.

Additionally, the analysis of the instantaneous stability criterion merits particular attention. Figure 27 illustrates the stability criterion of Den Hartog, derived from the instantaneous fluid force coefficients as a function of the relative angle of attack for different values of reduced velocity (U^*). Notably, the instantaneous stability parameter, $\beta_{inst} = \partial C_y/\partial\alpha' = -\partial C_L/\partial\alpha' - C_D$, exhibits both symmetry and an evident trend; its magnitude increases with the reduced velocity. This trend highlights that as U^* rises, the body becomes progressively more susceptible to galloping-like oscillations due to soft excitation. Consequently, the system transitions to an unstable regime from the perspective of a soft oscillator, indicating the potential for galloping to occur from rest.

The quasi-steady model does not capture the effects of vortex shedding, which occurs as a single vortex is shed each half-cycle of motion, as shown in figure 19, and is likely to be contributing to the motion of the body. Instead, the quasi-steady model focuses on the geometry of the body and movement-induced excitation, neglecting vortex shedding effects that significantly influence the fluid–structure interaction. This explains

https://doi.org/10.1017/jfm.2025.10866 Published online by Cambridge University Press

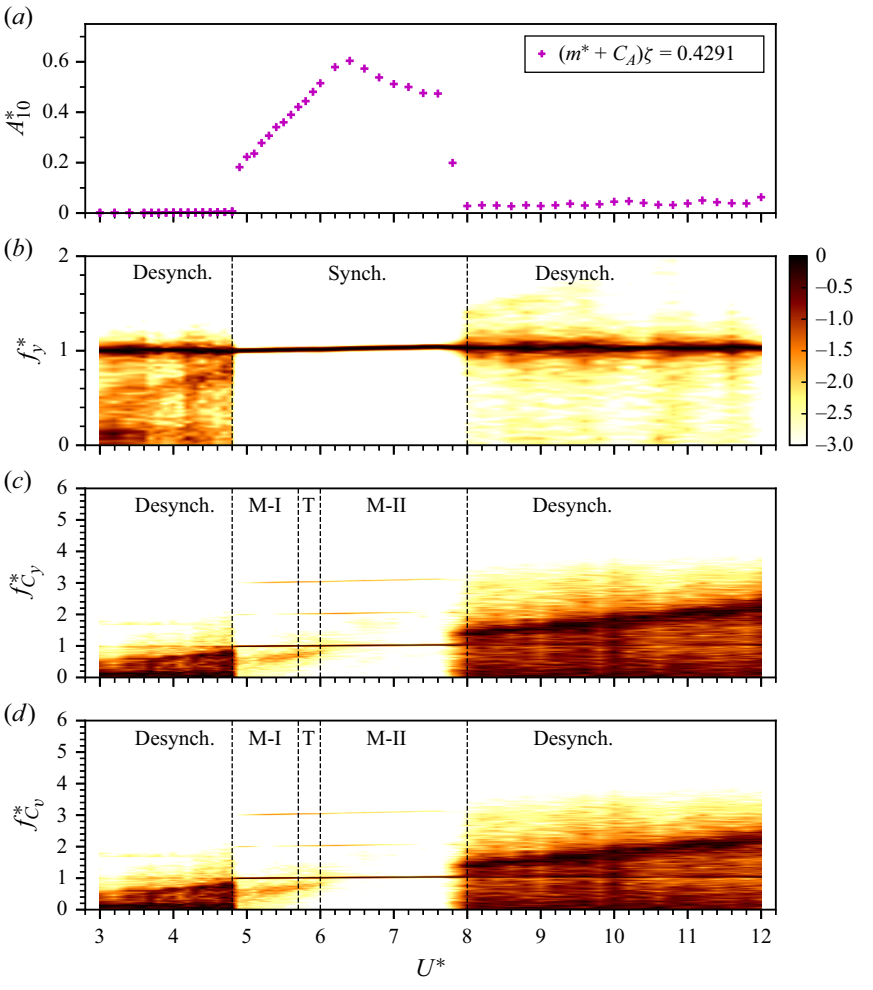


Figure 28. (*a*) A^*_{10} amplitude response and (*b–d*) logarithmic-scale PSD contours of normalised frequency responses as a function of reduced velocity for the $\epsilon = 2.00$ case with $(m^* + C_A)\zeta = 0.4291$. In panels (*b*)–(*d*), the vertical dashed lines represent the boundaries of the response regimes.

the discrepancies between the quasi-steady model and instantaneous force measurements. In summary, the energy transfer analysis based on the instantaneous force measurements suggests that the oblate spheroid is susceptible to a galloping-like response. Therefore, from the quasi-steady perspective, this spheroid case ($\epsilon = 2.00$) is not susceptible to classical transverse galloping from rest. However, based on the extrapolation of the stability criterion (Den Hartog's) applied on instantaneous fluid forcing, this spheroid can exhibit galloping oscillations, as indicated by the α'_{max} values and the amplitude growth at high U^*. This consideration motivates our use of the term 'galloping-like' rather than classical transverse galloping.

3.5. *VIV response at high mass-damping parameter value (Group II, $\epsilon = 2.00$)*

3.5.1. *Vibration response*

The case of $(m^* + C_A)\zeta = 0.4291$ represents a high mass-damping parameter configuration exhibiting a dynamic response composed of VIV only. Figure 28(*a*)

https://doi.org/10.1017/jfm.2025.10866 Published online by Cambridge University Press

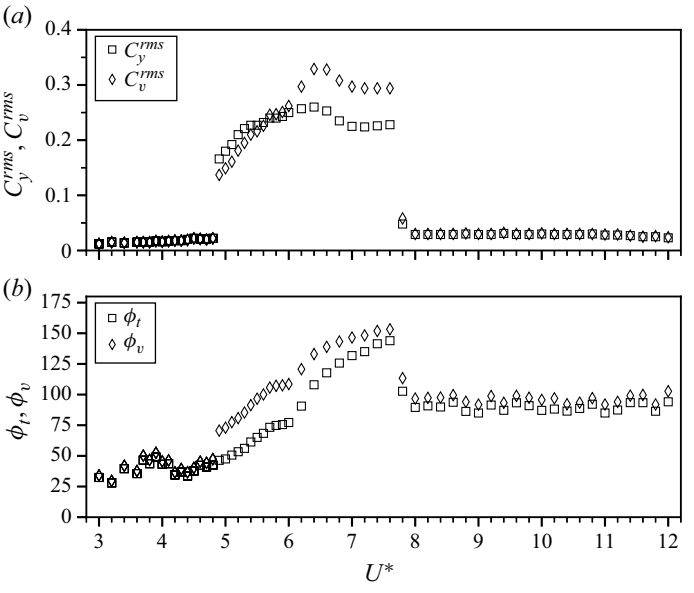


Figure 29. Variation of the (a) transverse lift force coefficient (C_y^{rms}) and vortex force coefficient (C_v^{rms}), and (b) total phase (ϕ_t) and vortex phase (ϕ_v), all as functions of the reduced velocity U^* for the $\epsilon = 2.00$ case with$(m^* + C_A)\zeta = 0.4291$.

demonstrates that the amplitude of vibration is typical of a VIV response that has been observed in the case of elastically mounted spheres immersed in water or air (see Govardhan & Williamson 2005; Rajamuni *et al.* 2018; Sareen *et al.* 2018*a*). Over the lock-in region, the maximum amplitude of vibration is $A_{10}^* = 0.6$ at $U^* = 6.4$. The frequency response of the oblate spheroid displacement (figure 28*b*) reveals that over the range $4.8 \leqslant U^* \leqslant 8.0$, the displacement frequency (f_y^*) is equal to the natural frequency of the system (f_{nw}). Based on the frequency responses of the fluid forces, two distinct vibration regimes can be associated with the VIV region: M-I and M-II. Mode I extends over the range $4.8 \leqslant U^* \leqslant 5.8$, where the frequency response of the fluid forces displays the stronger contribution at $f_{C_y}^* = f_{C_v}^* = 1$ and a weaker third harmonic contribution at $f_{C_y}^* = f_{C_v}^* = 3$.

In figure 29(*b*), it can be seen that the values of C_y^{rms} and C_v^{rms} suddenly jump from 0.05 to 0.15 in the range $4.8 \leqslant U^* \leqslant 5.0$, marking the onset of M-I. Within this U^* range, ϕ_v grows from $\sim 50°$ to $\sim 75°$. Additionally, ϕ_t leads by 30°, maintaining the same trend as ϕ_v.

With further increase in the reduced velocity, at $U^* \geqslant 6.0$, there is the appearance of a weak second harmonic in the spectra of the fluid forces, indicating a transition between VIV modes (see figure 28*c*,*d*). Based on the variation of the fluid forces and phases in figure 29, the onset of this second vibration is marked by a jump in the value of the total and vortex phases, where ϕ_t increases from $\sim 75°$ to $\sim 145°$ and ϕ_v from $\sim 110°$ to $\sim 150°$. The maximum amplitude of vibration is $A_{10}^* = 0.6$ at $U^* = 6.4$ (see figure 29*a*); this point is associated with a global maximum in the vortex force coefficient, $C_v^{rms} = 0.33$. The end of the VIV region is marked by a sudden drop in the values of the total and vortex phases from $\sim 150°$ to $\sim 90°$ at $U^* = 8.0$, marking the onset of the desynchronisation region.

https://doi.org/10.1017/jfm.2025.10866 Published online by Cambridge University Press

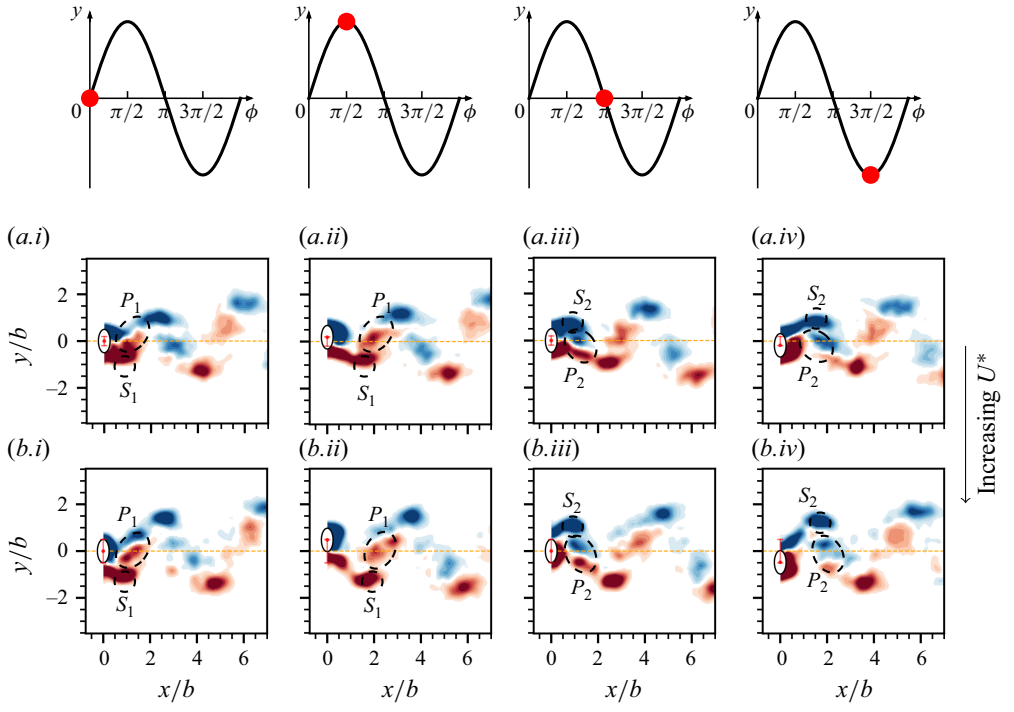


Figure 30. Wake patterns visualised from PIV spot measurements within the M-I regime for the $\epsilon = 2.00$ case with $(m^* + C_A)\zeta = 0.4291$ at (*a*) $U^* = 5.0$ and (*b*) $U^* = 6.0$. The red point on the sine waves shows the corresponding position of the spheroid during the oscillation cycle. The movie images are included in the supplementary material to help the reader understand the wake structure formation for the oscillating oblate spheroid.

3.5.2. *Wake modes*

Figure 30 shows phase-averaged PIV snapshots for M-I for two different reduced velocities of $U^* = [5, 6]$ for the high-damped case of $(m^* + C_A)\zeta = 0.4291$, where the FIV response exhibits VIV only. Increasing the damping ratio does not affect the wake pattern seen for M-I, which is still a $2(P + S)$ pattern, characterised by a pair (P) of opposite-sign vortices along with one single vortex (S) shed during half of an oscillation cycle. However, an increase in the damping ratio induces a notable decrease in the vibration range.

Figure 31 shows that the displacement and fluid force coefficients are highly periodic in this mode, with the fluid force coefficients, C_y and C_v, being in phase with the body displacement. The PSD plots reveal a behaviour similar to compared with those for $(m^* + C_A)\zeta = 0.1263$ (figure 16), where the main frequency contribution is at $f^* = 1$, while noting an additional strong component at $f^* = 3$.

Figure 32 illustrates the wake structure displayed by the spheroid for M-II at $U^* = 7.0$. In this case, even though the damping ratio has been incremented, the wake still exhibits a $2(P + S)$ wake pattern, as seen for $(m^* + C_A)\zeta = 0.1263$ (see § 3.3). Analogous to what has been discussed for the low damping case, the main difference with M-I is a greater deflection angle of the wake, along with an elongation of the shear layer. During the first half of the oscillation cycle, a pair of counter-rotating vortices (P_1) is shed along with a single vortex (S_1); it is worth noting that the vortices have similar intensities. In the second half of the oscillation cycle, there is a second pair of counter-rotating vortices (P_2) along with a single vortex (S_2) shed. The wake is very similar to the topology observed in

https://doi.org/10.1017/jfm.2025.10866 Published online by Cambridge University Press

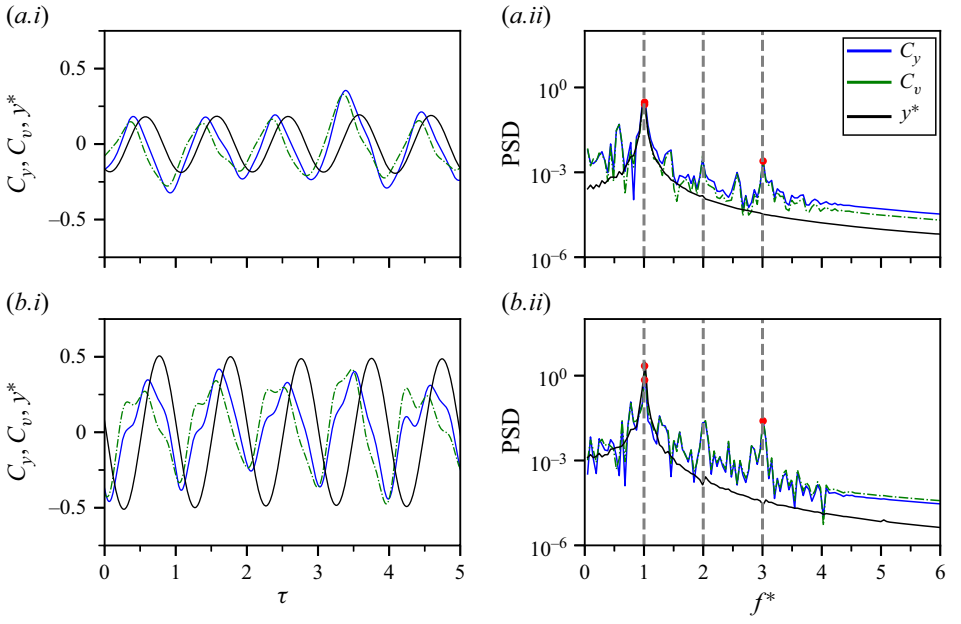


Figure 31. Sample time traces of the body displacement (y^*), and the coefficients of the total transverse force (C_y) and the vortex force (C_v) within the M-I regime, along with the corresponding frequency PSD plots for the $\epsilon = 2.00$ case with $(m^* + C_A)\zeta = 0.4291$ at (a) $U^* = 5.0$ and (b) $U^* = 6.0$.

figure 15 at $U^* = 8.0$, suggesting that M-II persists, even though the structural damping ratio has been increased significantly.

Figure 33 shows that the transverse and vortex forces are notably out of phase with the body displacement, similar to the behaviour observed for the low-damped case $(m^* + C_A)\zeta = 0.1263$. The frequency PSD plots display the presence of a main peak matching the body vibration frequency at $f^* = 1$ and an additional third harmonic contribution of weak power.

Figure 34 summarises the effect of damping ratio on the amplitude response through a contour map in $U^* - (m^* + C_A)\zeta$ parameter space. This clearly demonstrates that high vibration amplitudes are observed for low damping ratio and that as the damping ratio is increased, there is both a reduction in the peak amplitude as well as a reduction in the synchronisation U^* range. Together with the measured variations of the fluid forces and phases, it is possible to identify the regions of parameter space occupied by Modes I, II and G-I.

3.6. *FIV response of a thin oblate spheroid of* $\epsilon = 3.20$

In this subsection, the FIV response of an elastically mounted thin oblate spheroid of $\epsilon = 3.20$ is presented. Figure 35 illustrates the A^*_{10} response as a function of U^* for various values of $(m^* + C_A)\zeta$. It can be clearly seen that for $0.2289 \leqslant (m^* + C_A)\zeta \leqslant 0.5750$, the range of U^* associated with lock-in is greatly affected by an increase in $(m^* + C_A)\zeta$. However, the value of U^* marking the onset of FIV lies between 5.0 and 5.2, indicating that the start of the VIV region is not significantly influenced by a variation in the mass-damping parameter range tested. However, the maximum vibration amplitude is strongly affected, changing from $A^*_{10} \simeq 1.90$ for the lowest value of $(m^* + C_A)\zeta = 0.2289$ to $A^*_{10} = 0.75$ for the case of $(m^* + C_A)\zeta = 0.2959$. This represents a ~48 % decrease.

https://doi.org/10.1017/jfm.2025.10866 Published online by Cambridge University Press

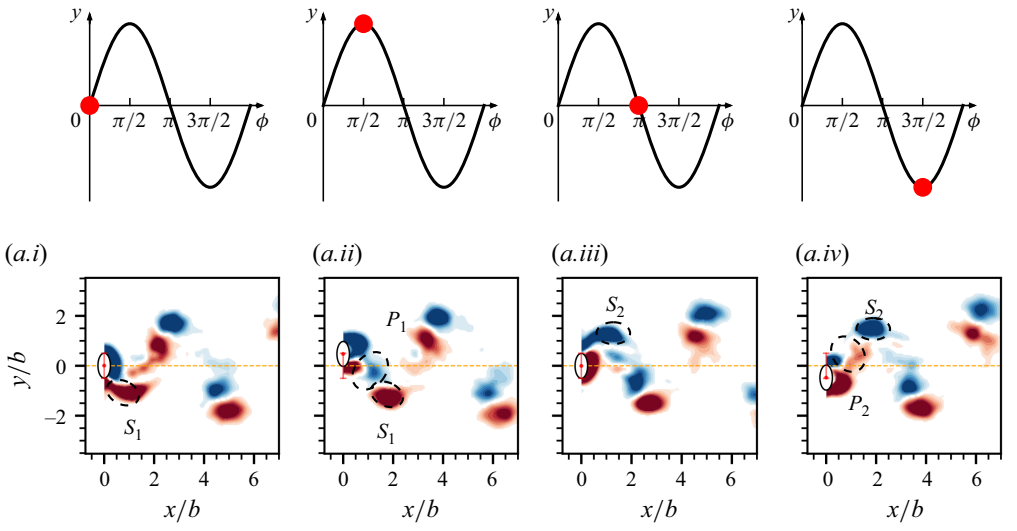


Figure 32. Wake patterns visualised from PIV spot measurements within M-II regime for the $\epsilon = 2.00$ case with $(m^* + C_A)\zeta = 0.4291$ at $U^* = 7.0$. The red point on the sine waves shows the corresponding position of the spheroid during the oscillation cycle. The movie images are included in the supplementary material to help the reader understand the wake513 structure formation for the oscillating oblate spheroid.

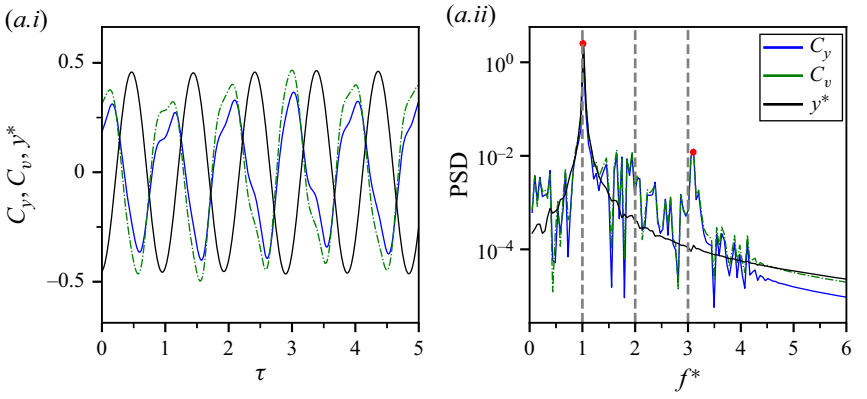


Figure 33. Sample time traces of the body displacement (y^*), and the coefficients of the total transverse force (C_y) and the vortex force (C_v) within the M-II regime, along with the corresponding frequency PSD plots for the $\epsilon = 2.00$ case with $(m^* + C_A)\zeta = 0.4291$ at $U^* = 7.0$.

For $(m^* + C_A)\zeta \geqslant 0.5750$, the maximum vibration is found to be $A^*_{10} < 0.05$, almost a full suppression.

Figure 36 displays the PSD contour plots of f^*_y, $f^*_{C_y}$ and $f^*_{C_v}$ as a function of U^* for the lowest the mass-damping parameter tested, $(m^* + C_A)\zeta = 0.2289$. Figure 36($a$) reveals that two main vibration regimes can be identified: VIV and VIV-like (as suggested by Cordero Obando *et al.* 2024). The VIV regime occurs over $5.2 \leqslant U^* \leqslant 6.5$ and the VIV-like regime over $7.0 \leqslant U^* \leqslant 9.6$.

The onset of the VIV regime is marked by a major jump in the amplitude response, from $A^*_{10} \leqslant 0.05$ at $U^* = 5.0$ to $A^*_{10} = 1.0$ at $U^* = 5.2$ (figure 36a). Similar to the cases of $\epsilon = 1.00$ and 2.00 with similar $(m^* + C_A)\zeta$ values, the onset of VIV is within the range of

https://doi.org/10.1017/jfm.2025.10866 Published online by Cambridge University Press

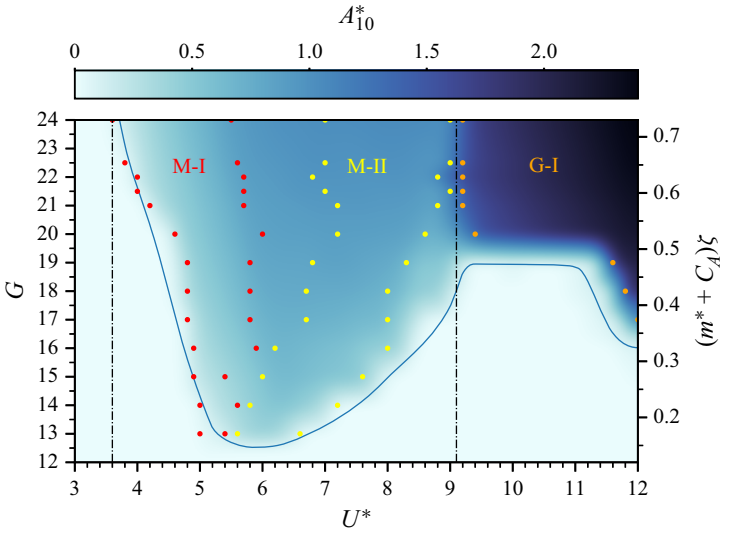


Figure 34. FIV amplitude response contour map for an oblate spheroid of $\epsilon = 2.00$ in $(U^*, (m^* + C_A)\zeta, G)$ parameters space. Note that G corresponds to the gap distance in mm, which is directly related to the mass-damping parameter, $(m^* + C_A)\zeta$, shown on the right axis. The vertical dash-dotted lines display the boundary between VIV and galloping. The region within the red dot boundary (•) corresponds to M-I, the yellow dots boundary (•) demarcates M-II and the orange dot boundary (•) corresponds to mode G-I.

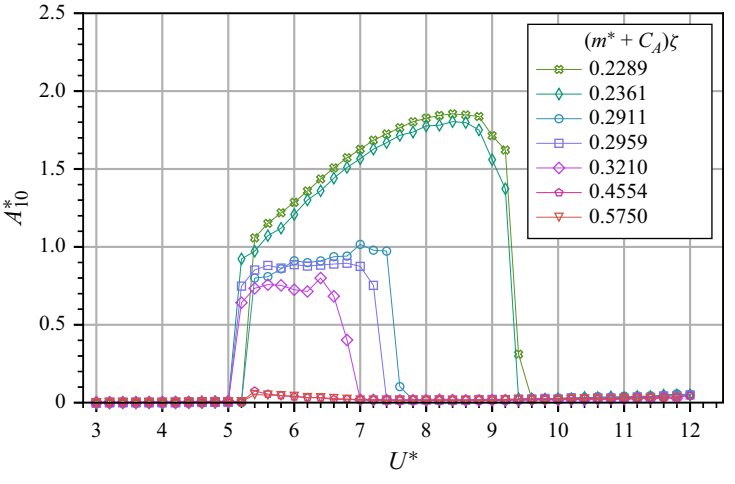


Figure 35. A^*_{10} amplitude response as a function of U^* for $\epsilon = 3.20$ with various values of $(m^* + C_A)\zeta$.

$4.0 \leqslant U^* \leqslant 5.0$. Furthermore, over the range $5.2 \leqslant U^* \leqslant 6.6$, the displacement frequency (f^*_y), the total transverse force frequency ($f^*_{C_y}$) and the vortex force frequency ($f^*_{C_v}$) show a single dominant frequency component close to the natural frequency of the system (f_{nw}) (figure 36*b*,*c*,*d*), indicating a typical VIV synchronisation. Thus, the first mode of vortex formation is dominated by VIV, termed Mode I (M-I). A detailed discussion of the harmonics (i.e. the second and third) observed in both $f^*_{C_y}$ and $f^*_{C_v}$, and their association with $2(2P + S)$ wake patterns, is provided by Cordero Obando *et al.* (2024).

https://doi.org/10.1017/jfm.2025.10866 Published online by Cambridge University Press

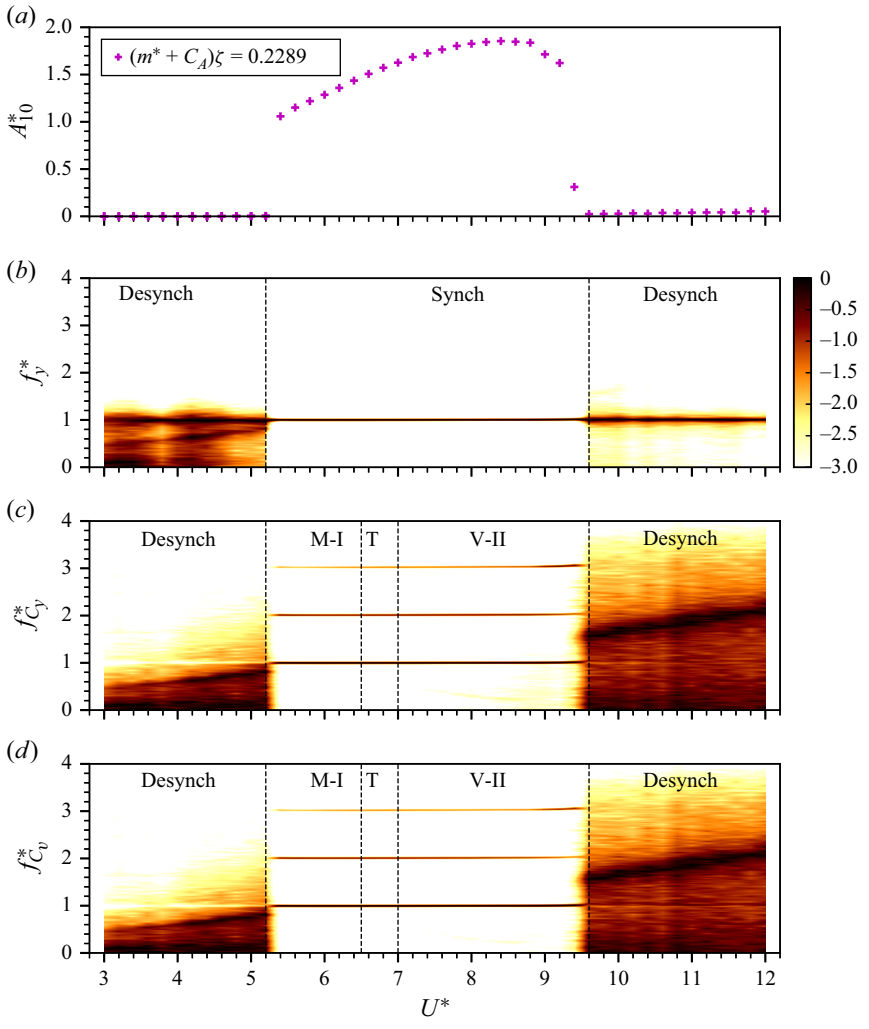


Figure 36. (*a*) A^*_{10} amplitude response and (*b–d*) the logarithmic-scale normalised frequency PSD contours as a function of U^* for $\epsilon = 3.20$ with $(m^* + C_A)\zeta = 0.2289$. In panels (*b*)–(*d*), the vertical dashed lines represent the boundaries of the response regimes.

Figure 37 displays the variations of the root-mean-square coefficients of the fluid forces (C_y^{rms} and C_v^{rms}) and phases (ϕ_t and ϕ_v) as a function of U^*. The start of M-I is induced by a sudden jump of the fluid force coefficients at $U^* = 4.8$ and then progressively rises until a first magnitude peak is reached. The total phase (ϕ_t) is almost constant at 25° over the range $3.6 \leqslant U^* \leqslant 6.6$, while the vortex phase (ϕ_v) varies slightly between 70° and 75° over the same range.

With a further increase in the reduced velocity ($U^* \geqslant 6.6$), the vibration amplitude response transitions towards a plateau, with A^*_{10} very close to 1.9, marking the appearance of another vortex mode of formation, termed V-II (see figure 36). This mode displays a distinct frequency response compared with M-II; in particular, there is a significant contribution of a harmonic at two times the body oscillation frequency, $2f^*_y$, in both the transverse and vortex force frequency responses, and a less powerful contribution coming from an additional harmonic at three times the body oscillation frequency, $3f^*_y$. The end

https://doi.org/10.1017/jfm.2025.10866 Published online by Cambridge University Press

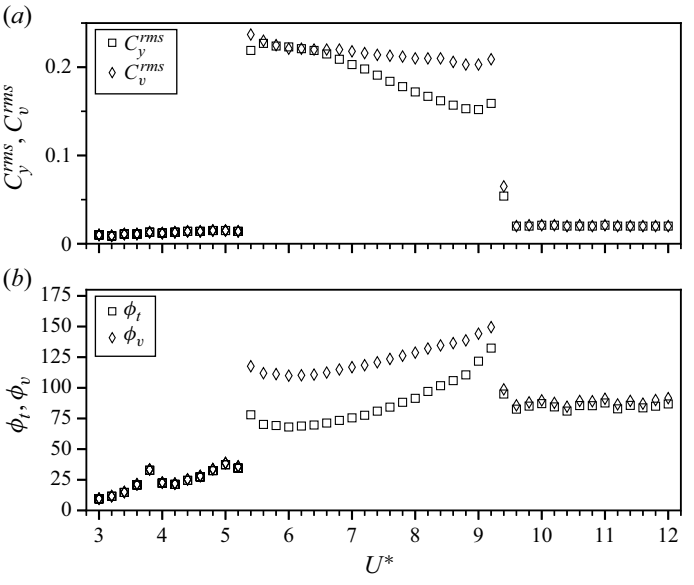


Figure 37. Variation of (a) the coefficients of the transverse and vortex forces (C_y^{rms} and C_v^{rms}), and (b) the total and vortex phases (ϕ_t and ϕ_v), all as functions of reduced velocity U^* for $\epsilon = 3.20$ with $(m^* + C_A)\zeta = 0.2289$.

of V-II is marked by a noticeable step (i.e. kink) in the frequency responses of $f^*_{C_y}$ and $f^*_{C_v}$ at $3f^*_y$ for the value of $U^* = 9.0$. It is noteworthy that for V-II, the highest amplitude frequency component is still the one equal to the displacement frequency, f^*_y, suggesting that the FIV responsible for the vibration is associated with VIV.

Figure 37 reveals that the value of C_y^{rms} decreases progressively from its peak 0.22 at $U^* = 5.4$ towards 0.2 at $U^* = 7.0$, indicative of a transition between VIV modes. For mode M-I, ϕ_t remains pretty much constant at 75° over the range $5.2 \leqslant U^* \leqslant 7.0$, and then grows almost linearly from $\sim 75°$ to 125° in the range $7.0 \leqslant U^* \leqslant 9.4$, associated with mode V-II. Similarly, ϕ_v displays a marked jump at $U^* = 5.2$ and then grows slowly from 125° at the start of mode M-I until it reaches a maximum value of 150° at $U^* = 9.4$. This is similar to the phase relationship seen for VIV of a sphere, consistent with this oscillation remaining VIV-dominated (see Govardhan & Williamson 2005).

3.7. *Power extraction from FIV of the spheroids*

3.7.1. *An optimal damping ratio for maximum average power coefficient*

For an elastically mounted sphere undergoing structural vibration, it is possible to harvest energy from the flow by adding a structural damper. In practice, this damping can be supplied by an electrical generator. The instantaneous power output of the spheroid can be calculated as $P = F_y \cdot \dot{y}$, where $\dot{y}$ is the velocity of the spheroid. Assuming the structural vibration is periodic, this can be approximated by $P = c\dot{y}^2$ (Zhao *et al.* 2022*a*). A lower damping ratio may result in higher vibration amplitude and body velocity $\dot{y}$; however, this does not necessarily correspond to a higher output power. Furthermore, a power output coefficient can be defined as

$$C_p = \frac{P}{\rho U^3 b^2 \pi/8}, \tag{3.10}$$

https://doi.org/10.1017/jfm.2025.10866 Published online by Cambridge University Press

where $\rho U^3 b^2 \pi/8$ is the fluid power passing through the projected spheroid surface area. Equation (3.10) demonstrates the energy that can be potentially extracted from the surrounding fluid flow via structural vibration. For a bluff body undergoing FIV, the time-average power coefficient can be expressed as

$$\overline{C_p} = \frac{1}{T}\int_0^T C_p(t)\,\mathrm{d}t. \tag{3.11}$$

Here, T is the integration time spanning many oscillation cycles.

Figure 38 illustrates the variation of the time-average power coefficient as a function of reduced velocity for various values of the mass-damping parameter and aspect ratio. For all cases ($\epsilon = 1.00, 2.00, 3.20$), there is a specific damping ratio where the power coefficient reaches its maximum. As shown in figure 39, the optimal damping ratio for energy harvesting varies slightly with geometry. For the sphere case, the maximum power output occurs at $(m^* + C_A)\zeta = 0.1401$. For $\epsilon = 2.00$, the optimal value is $\zeta = 0.2679$, while the thinnest oblate spheroid ($\epsilon = 3.20$) achieves its peak performance at $\zeta = 0.2726$.

Interestingly, while the optimal mass-damping parameter across different geometries remain similar, the maximum values of $\overline{C_p}$ vary significantly. The sphere achieves a peak of 0.021 at $U^* = 8.6$, the oblate spheroid ($\epsilon = 2.00$) reaches 0.10 at $U^* = 6.0$, and the thinnest spheroid ($\epsilon = 3.20$) attains the highest value of 0.175 at $U^* = 6.8$. Additionally, as the afterbody size decreases, less damping is required to minimise or attenuate the potential of energy harvesting from FIV.

The oblate spheroid with $\epsilon = 2.00$ demonstrates robust performance, maintaining $\overline{C_{p_{max}}}$ values in the range $0.075 \leqslant \overline{C_{p_{max}}} \leqslant 0.10$ over a broad range of mass-damping parameters ($0.1263 \leqslant (m^* + C_A)\zeta \leqslant 0.2012$). In contrast, the thinnest spheroid ($\epsilon = 3.20$) achieves a higher power coefficient but within a narrower range of the mass-damping parameter, highlighting the trade-off between peak performance and operational range. As demonstrated by Cordero Obando *et al.* (2024), the energy extraction performance of spheroids is influenced by two primary parameters: the damping ratio, which optimises energy extraction from the flow, and the aspect ratio.

It can be concluded that the maximum average power coefficient is found over the range of reduced velocity U^* corresponding to the VIV region regardless of the value of $(m^* + C_A)\zeta$; however, the power output decreases quickly moving away from the corresponding U^* value. Over the galloping-dominated U^* range, the average power coefficient $\overline{C_P}$ remains almost constant. Consequently, the potentially extractable power from the galloping region may be more suitable for engineering applications. Galloping behaviour has been advantageous for practical applications (see Barrero-Gil, Alonso & Sanz-Andres 2010; Vicente-Ludlam, Barrero-Gil & Velazquez 2014; Hémon *et al.* 2017) due to the stability of power output. In comparison, the maximum power coefficient for a circular cylinder undergoing VIV is ∼0.18 (Bernitsas *et al.* 2008; Soti *et al.* 2018). While the maximum power coefficient of the spheroid is below that of the circular cylinder, which has been used as a renewable energy harvesting device (Bernitsas *et al.* 2008), the current investigation indicates an improvement in $\overline{C_p}$ over that of a sphere. Indeed, Cordero Obando *et al.* (2024) shows that increasing the aspect ratio of the spheroid to 3.20, increases the power coefficient to 0.165, which is almost comparable to the circular cylinder case. Of note, the Betz limit – derived from an actuator disk theory using the rotor swept area as the reference area (see Betz 1966) – establishes an upper limit of 16/27 for the power coefficient of such devices. Of course, adding elastically mounted spheroids in the wake of those upstream may increase the energy extraction potential – as occurs in wind turbine-based wind farms. It may also be possible to place coupled spheroids

https://doi.org/10.1017/jfm.2025.10866 Published online by Cambridge University Press

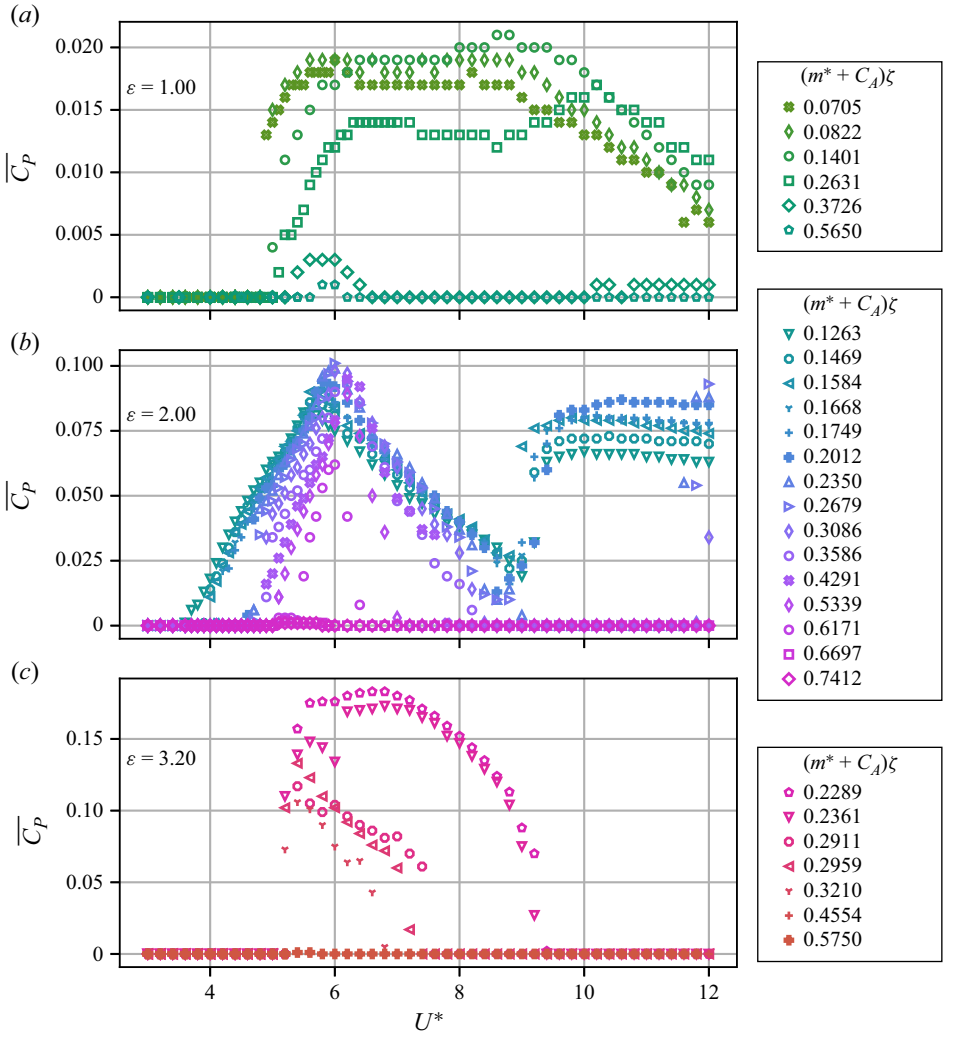


Figure 38. Variations the time-average power coefficient ($\overline{C_p}$) as a function of reduced velocity for (a) $\epsilon = 1.00$, (b) $\epsilon = 2.00$ and (c) $\epsilon = 3.20$, with various values of $(m^* + C_A)\zeta$.

aligned cross-stream to extract further energy – again noting that adding blades increases the efficiency of wind turbines. While these aspects are not within the scope of the current study, it is of interest that such a compound device already exists for elastically mounted circular cylinders (Bernitsas *et al.* 2008; Kim & Bernitsas 2016).

4. Galloping-like vibration for $\epsilon = 2.00$ at higher U^*

Finally, a broader range of reduced velocities was investigated using different spring combinations to assess whether the galloping-like response would continue beyond the U^* range already tested.

The maximum reduced velocity achieved was $U^* = 31.8$. It can be seen that depending on the value of the natural frequency of the system, the transition between these FIV mechanisms is either gradual or separated by a desynchronised region.

https://doi.org/10.1017/jfm.2025.10866 Published online by Cambridge University Press

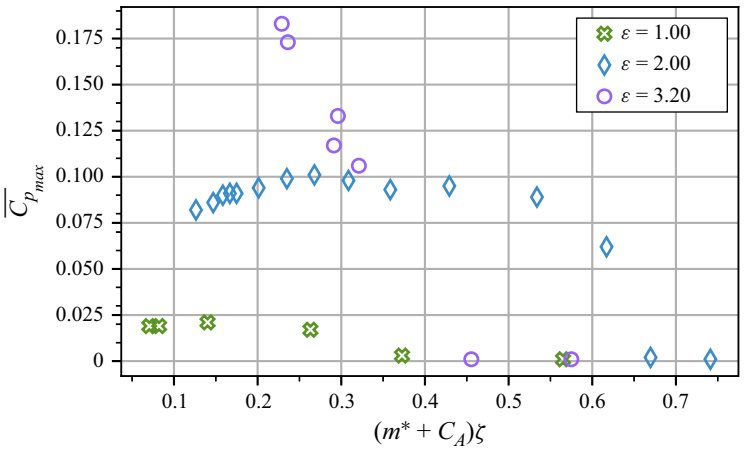


Figure 39. Variation of the maximum average power coefficient, $\overline{C_{p_{max}}}$, as a function of the damping ratio, ζ, for various aspect ratios, ϵ.

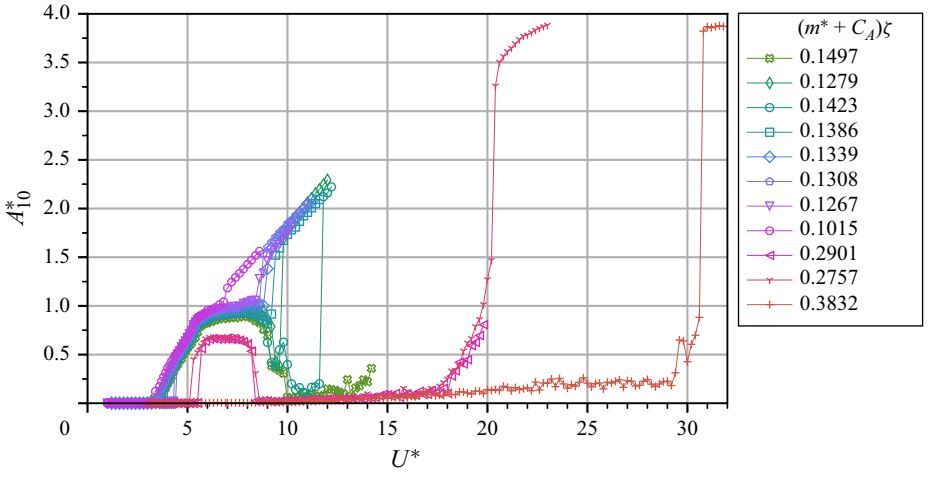


Figure 40. A^*_{10} amplitude response as a function of reduced velocity for $\epsilon = 2.00$ with various values of $(m^* + C_A)\zeta$.

Figure 40 shows the A^*_{10} amplitude response as a function of U^* for various mass-damping parameter values. For the case of $(m^* + C_A)\zeta = 0.3832$, the dynamic response over a wide U^* range displayed desynchronised behaviour, displaying intermittent vibration bursts, similar to Mode IV of vibration for a sphere (Rajamuni *et al.* 2018). However, a relatively sudden significant amplitude increase was observed approaching $U^* = 30$, where the vibration amplitude peaked at $A^*_{10} = 3.7$.

Figure 41 provides a detailed analysis of the case $(m^* + C_A)\zeta = 0.2757$, which also displays a high amplitude of vibration region ($A^*_{10} \geqslant 3$). As shown in figure 41(*b*), lock-in occurs over the ranges $4.8 \leqslant U^* \leqslant 8.2$ for the VIV response and $18 \leqslant U^* \leqslant 27$ for the high-amplitude galloping-like oscillations. Figure 41(*c*) illustrates that the frequency of the transverse force coefficient, $f^*_{C_y}$, follows the Strouhal frequency, f^*_{vo}, for a fixed oblate spheroid. This behaviour results in a desynchronised region characterised by a significant

https://doi.org/10.1017/jfm.2025.10866 Published online by Cambridge University Press

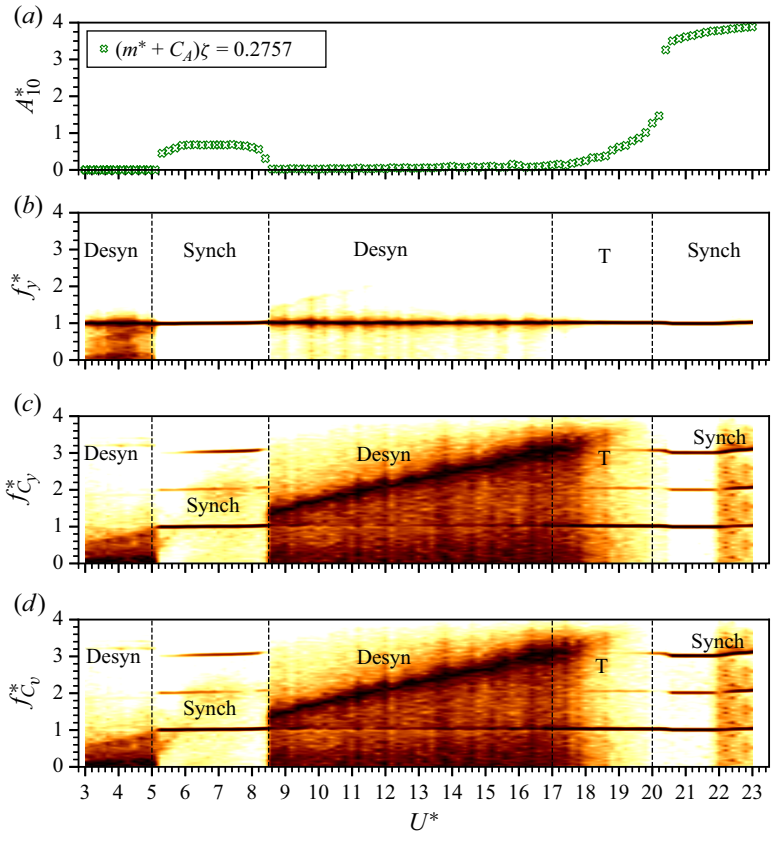


Figure 41. (*a*) Amplitude response and (*b–d*) logarithmic-scale normalised frequency power spectral density (PSD) contours as a function of U^* for $\epsilon = 2.00$ with $(m^* + C_A)\zeta = 0.2757$. In panels (*b*)–(*d*), the vertical dashed lines represent the boundaries of the response regimes.

attenuation in vibration amplitude. Similar to the other cases examined, the VIV region can be further divided into two distinct vortex-shedding modes, referred to as Mode I and Mode II. Mode I is identified by the presence of a single dominant harmonic, while Mode II is distinguished by the emergence of a third harmonic. In contrast, the galloping-like oscillation region exhibits a pronounced contribution from both the second and third harmonics, which drive the high-amplitude oscillations observed in this range.

Figure 42 illustrates the variation of the total transverse force and vortex force coefficients, along with the corresponding total and vortex phases, as functions of the reduced velocity for $(m^* + C_A)\zeta = 0.2757$. The onset of the VIV response is marked by a sudden increase in the root-mean-square coefficient of the transverse force, C_y^{rms}. This value peaks during Mode I and then progressively decreases as the system transitions to Mode II. During Mode I, the total phase, ϕ_t, remains at approximately 30° and gradually increases to 150° at the peak amplitude of Mode II. This is followed by a sharp decrease to approximately 100°, coinciding with the desynchronised region. Beyond this transition, the total phase stabilises at approximately 30° before abruptly rising to 140°, corresponding to the high-amplitude vibration regime. Notably, the region of high-amplitude vibrations is characterised by a substantial increase in the total transverse force coefficient, which rises sharply from 0.2 to 0.5.

https://doi.org/10.1017/jfm.2025.10866 Published online by Cambridge University Press

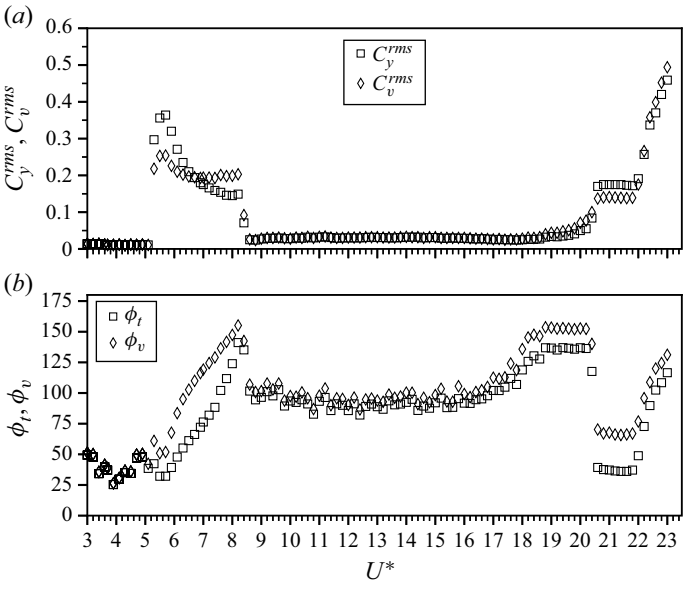


Figure 42. Variations of (*a*) coefficients of the transverse and vortex forces, and (*b*) total and vortex phases, all as functions of reduced velocity for $\epsilon = 2.00$ with $(m^* + C_A)\zeta = 0.2757$.

5. Conclusions

A detailed analysis has been undertaken of the vibration response, fluid forces and phases as a function of reduced velocity for a 1 degree-of-freedom elastically mounted oblate spheroid of $m^* = 25$ and aspect ratio $\epsilon = 2.00$. The measurements were recorded over the reduced velocity range $3.0 \leqslant U^* \leqslant 12.0$, incrementing the velocity in small steps from the previous settled state. This corresponds to the Reynolds number range $4930 \leqslant Re \leqslant 19\,690$. The dynamic response of a sphere ($\epsilon = 1.00$) was also investigated to provide a reference point and comparison with this spheroid case. Finally, a more restricted analysis of the high aspect ratio $\epsilon = 3.20$ spheroid case was undertaken to examine the sensitivity of the findings to aspect ratio.

The study examined the effect of the structural damping ratio, ζ, on the FIV response of the $\epsilon = 2.00$ spheroid. As discussed in § 3, the FIV responses could be classified into two groups, determined by whether VIV and a galloping-like response occurred (Group I – for lower damping ratios) or just VIV (Group II – for higher damping). Of particular interest is the presence of a galloping-dominated response, which is very similar to the galloping response of a non-rotationally symmetric 2-D bluff body (e.g. a square or elliptical cylinder). For those values of ζ within group II, the dynamic response mainly comprised VIV with the galloping-like response fully suppressed. It was observed through PIV measurements that the VIV region is composed of two different vortex modes of formation, Mode I and Mode II, partially delineated by phase and fluid force differences. In contrast, the galloping response is associated with Mode G-I.

The energy harvesting performance for the oblate spheroid was analysed for different values of ζ and aspect ratios ($\epsilon = 1.00$, 2.00 and 3.20). The maximum average power coefficient was found for an optimal combination of structural damping ratio, reduced velocity and aspect ratio. For the case, $\epsilon = 2.00$, despite lower amplitude oscillations, the maximum average power coefficient occurred in the VIV region with $\overline{C_p} = 0.10$. Of interest in the galloping-like regime was the behaviour of the average power coefficient,

https://doi.org/10.1017/jfm.2025.10866 Published online by Cambridge University Press

which remained almost constant over the entire range of reduced velocities examined. Indeed, this average power coefficient was only 25 % lower than the VIV maximum. This suggests that an oblate spheroid undergoing galloping-like oscillations may be a candidate for harvesting energy from fluid flows at a high Reynolds number, especially noting that higher-aspect-ratio spheroids have been shown to provide a power coefficient approaching that of a circular cylinder. It is also worth noting that the compact nature of an oblate spheroid may be favourable for specific engineering energy harvesting applications.

By comparing the dynamic response of an oblate spheroid of aspect ratio, $\epsilon = 2.00$, with that of a sphere ($\epsilon = 1.00$) (e.g. Govardhan & Williamson 2005; Sareen *et al.* 2018*a*), it is clear that aspect ratio plays a strong role in the FIV response. This large amplitude vibration mode was related to a superharmonic forcing frequency (of the transverse lift force component), which corresponds to three times the natural frequency of the oblate spheroid. Hence, a 3-D flow field visualisation in the wake would be beneficial to compare the wake structure of the present case to that of a sphere. Other spring stiffnesses can be tested to establish a relation between the power output and the Reynolds number. Finally, the quasi-steady theory could be applied in further studies to predict and measure the aerodynamic force driving the galloping-like response.

Supplementary movies. Supplementary movies are available at https://doi.org/10.1017/jfm.2025.866.

Funding. This work was supported by the Australian Research Council (Discovery Early Career Research Award DE200101650 and Discovery Project grant DP210100990).

Declaration of interest. The authors report no conflict of interest.

References

Barrero-Gil, A., Alonso, G. & Sanz-Andres, A. 2010 Energy harvesting from transverse galloping. *J. Sound Vib.* **329** (14), 2873–2883.

Bearman, P., Gartshore, I., Maull, D. & Parkinson, G. 1987 Experiments on flow-induced vibration of a square-section cylinder. *J. Fluids Struct.* **1** (1), 19–34.

Bearman, P.W. 1984 Vortex shedding from oscillating bluff bodies. *Annu. Rev. Fluid Mech.* **16**, 195–222.

Bernitsas, M.M., Raghavan, K., Ben-Simon, Y. & Garcia, E. 2008 VIVACE (Vortex induced vibration aquatic clean energy): a new concept in generation of clean and renewable energy from fluid flow. *J. Offshore Mech. Arctic Engng* **130** (4), 041101.

Betz, A. 1966 *Introduction to the Theory of Flow Machines*. Pergamon Press.

Blackburn, H.M., Marques, F. & Lopez, J.M. 2005 Symmetry breaking of two-dimensional time-periodic wakes. *J. Fluid Mech.* **522**, 395–411.

Blevins, R.D. 2001 *Flow-Induced Vibration*, 2nd edn. Krieger Publishing Company.

Bourguet, R. & Lo Jacono, D. 2015 In-line flow-induced vibrations of a rotating cylinder. *J. Fluid Mech.* **781**, 127–165.

Cheng, Z., Lien, F.-S., Dowell, E.H., Yee, E., Wang, R. & Zhang, J.H. 2023 Critical effect of fore-aft tapering on galloping triggering for a trapezoidal body. *J. Fluid Mech.* **967**, A18.

Choi, H., Jeon, W.-P. & Kim, J. 2008 Control of flow over a bluff body. *Annu. Rev. Fluid Mech.* **40**, 113–139.

Cordero Obando, A., Thompson, M.C., Hourigan, K. & Zhao, J. 2024 Effect of aspect ratio on flow-induced vibration of oblate spheroids and implications for energy generation. *J. Fluids Struct.* **128**, 104137.

Den Hartog, J. 1932 Transmission line vibration due to sleet. *Trans. Am. Inst. Elect. Engrs* **51** (4), 1074–1076.

Eshbal, L., Kovalev, D., Rinsky, V., Greenblatt, D. & van Hout, R. 2019*a* Tomo-PIV measurements in the wake of a tethered sphere undergoing VIV. *J. Fluids Struct.* **89**, 132–141.

Eshbal, L., Rinsky, V., David, T., Greenblatt, D. & van Hout, R. 2019*b* Measurement of vortex shedding in the wake of a sphere at Re = 465. *J. Fluid Mech.* **870**, 290–315.

Fouras, A., Lo Jacono, D. & Hourigan, K. 2008 Target-free Stereo PIV: a novel technique with inherent error estimation and improved accuracy. *Exp. Fluids* **44** (2), 317–329.

Govardhan, R. & Williamson, C.H.K. 2000 Modes of vortex formation and frequency response of a freely vibrating cylinder. *J. Fluid Mech.* **420**, 85–130.

https://doi.org/10.1017/jfm.2025.10866 Published online by Cambridge University Press

GOVARDHAN, R. & WILLIAMSON, C.H.K. 1997 Vortex-induced motions of a tethered sphere. *J. Wind Engng Ind. Aerodyn.* **69**, 375–385.

GOVARDHAN, R. & WILLIAMSON, C.H.K. 2005 Vortex-induced vibrations of a sphere. *J. Fluid Mech.* **531**, 11–47.

HÉMON, P., AMANDOLESE, X. & ANDRIANNE, T. 2017 Energy harvesting from galloping of prisms: a wind tunnel experiment. *J. Fluids Struct.* **70**, 390–402.

HOURIGAN, K., ZHAO, J., LEWEKE, T. & THOMPSON, M.C. 2026 Flow-induced vibration of bluff bodies. In *Volume 5: Nonlinear Dynamics and Vibrations: Applications in Engineering*, (ed. G. Rega), vol. 5, World Scientific.

VAN HOUT, R., EISMA, J., ELSINGA, G.E. & WESTERWEEL, J. 2018 Experimental study of the flow in the wake of a stationary sphere immersed in a turbulent boundary layer. *Phys. Rev. Fluids* **3**, 024601.

JAUVTIS, N., GOVARDHAN, R. & WILLIAMSON, C.H.K. 2001 Multiple modes of vortex-induced vibration of a sphere. *J. Fluids Struct.* **15** (3), 555–563.

KIM, E.S. & BERNITSAS, M.M. 2016 Performance prediction of horizontal hydrokinetic energy converter using multiple-cylinder synergy in flow induced motion. *Appl. Energy* **170**, 92–100.

KOVALEV, D., ESHBAL, L. & VAN HOUT, R. 2022 Three-dimensional flow field measurements in the wake of a tethered sphere crossing the onset of vortex induced vibrations. *J. Fluid Mech.* **943**, A37.

LIGHTHILL, J. 1986 *An Informal Introduction to Theoretical Fluid Mechanics*. Clarendon Press.

LIMACHER, E., MORTON, C. & WOOD, D. 2018 Generalized derivation of the added-mass and circulatory forces for viscous flows. *Phys. Rev. Fluids* **3** (1), 014701.

LIMACHER, E.J. 2021 Added-mass force on elliptic airfoils. *J. Fluid Mech.* **926**, R2.

LO, J.C.C., HOURIGAN, K., THOMPSON, M.C. & ZHAO, J. 2023 The effect of structural damping on flow-induced vibration of a thin elliptical cylinder. *J. Fluid Mech.* **974**, A5.

LV, Y., SUN, L., BERNITSAS, M.M. & SUN, H. 2021 A comprehensive review of nonlinear oscillators in hydrokinetic energy harnessing using flow-induced vibrations. *Renew. Sustainable Energy Rev.* **150**, 111388.

MCQUEEN, T., ZHAO, J., SHERIDAN, J. & THOMPSON, M.C. 2020 Feedback control of flow-induced vibration of a sphere. *J. Fluid Mech.* **889**, A30.

MIRAUDA, D., VOLPE PLANTAMURA, A. & MALAVASI, S. 2014 Dynamic response of a sphere immersed in a shallow water flow. *J. Offshore Mech. Arctic Engng* **136** (2), 021101.

MISHRA, R., BHARDWAJ, R. & THOMPSON, M.C. 2024 The effect of structural damping on flow-induced vibration of a thin elliptical cylinder. *J. Fluid Mech.* **984**, A12.

NAUDASCHER, E. & ROCKWELL, D. 2005 *Flow-Induced Vibrations: An Engineering Guide*. Dover Publications.

NEMES, A., ZHAO, J., LO JACONO, D. & SHERIDAN, J. 2012 The interaction between flow-induced vibration mechanisms of a square cylinder with varying angles of attack. *J. Fluid Mech.* **710**, 102–130.

NOVAK, M. 1972 Galloping oscillations of prismatic structures. *J. Engng Mech. Div.* **98** (1), 27–46.

PARKINSON, G.V. & SMITH, J.D. 1964 The square prism as an aeroeslastic non-linear oscillator. *Q. J. Mech. Appl. Maths* **17** (2), 225–239.

RAJAMUNI, M.M., THOMPSON, M.C. & HOURIGAN, K. 2018 Transverse flow-induced vibrations of a sphere. *J. Fluid Mech.* **837**, 931–966.

RAJAMUNI, M.M., THOMPSON, M.C. & HOURIGAN, K. 2020 Vortex dynamics and vibration modes of a tethered sphere. *J. Fluid Mech.* **885**, A10.

SAREEN, A., ZHAO, J., LO JACONO, D., SHERIDAN, J., HOURIGAN, K. & THOMPSON, M.C. 2018*a* Vortex-induced vibration of a rotating sphere. *J. Fluid Mech.* **837**, 258–292.

SAREEN, A., ZHAO, J., SHERIDAN, J., HOURIGAN, K. & THOMPSON, M.C. 2018*b* Vortex-induced vibrations of a sphere close to a free surface. *J. Fluid Mech.* **846**, 1023–1058.

SOTI, A.K., THOMPSON, M.C., SHERIDAN, J. & BHARDWAJ, R. 2017 Harnessing electrical power from vortex-induced vibration of a circular cylinder. *J. Fluids Struct.* **70**, 360–373.

SOTI, A.K., ZHAO, J., THOMPSON, M.C., SHERIDAN, J. & BHARDWAJ, R. 2018 Damping effects on vortex-induced vibration of a circular cylinder and implications for power extraction. *J. Fluids Struct.* **81**, 289–308.

VICENTE-LUDLAM, D., BARRERO-GIL, A. & VELAZQUEZ, A. 2014 Optimal electromagnetic energy extraction from transverse galloping. *J. Fluids Struct.* **51**, 281–291.

WANG, J., GENG, L., DING, L., ZHU, H. & YURCHENKO, D. 2020*a* The state-of-the-art review on energy harvesting from flow-induced vibrations. *Appl. Energy* **267**, 114902.

WANG, J.-S., FAN, D. & LIN, K. 2020*b* A review on flow-induced vibration of offshore circular cylinders. *J. Hydrodyn.* **32** (3), 415–440.

WANG, Z., DU, L., ZHAO, J. & SUN, X. 2017 Structural response and energy extraction of a fully passive flapping foil. *J. Fluids Struct.* **72**, 96–113.

https://doi.org/10.1017/jfm.2025.10866 Published online by Cambridge University Press

WILLIAMSON, C.H.K. & GOVARDHAN, R. 1997 Dynamics and forcing of a tethered sphere in a fluid flow. *J. Fluids Struct.* **11** (3), 293–305.

WILLIAMSON, C.H.K. & GOVARDHAN, R. 2008 A brief review of recent results in vortex-induced vibrations. *J. Wind Engng Ind. Aerodyn.* **96** (6–7), 713–735.

WILLIAMSON, C.H.K. & ROSHKO, A. 1988 Vortex formation in the wake of an oscillating cylinder. *J. Fluids Struct.* **2** (4), 355–381.

ZHAO, J., HOURIGAN, K. & THOMPSON, M.C. 2018*a* Flow-induced vibration of D-section cylinders: an afterbody is not essential for vortex-induced vibration. *J. Fluid Mech.* **851**, 317–343.

ZHAO, J., LEONTINI, J.S., LO JACONO, D. & SHERIDAN, J. 2014*a* Chaotic vortex induced vibrations. *Phys. Fluids* **26** (12), 121702.

ZHAO, J., LEONTINI, J.S., LO JACONO, D. & SHERIDAN, J. 2014*b* Fluid–structure interaction of a square cylinder at different angles of attack. *J. Fluid Mech.* **747**, 688–721.

ZHAO, J., LO JACONO, D., SHERIDAN, J., HOURIGAN, K. & THOMPSON, M.C. 2018*b* Experimental investigation of in-line flow-induced vibration of a rotating cylinder. *J. Fluid Mech.* **847**, 664–699.

ZHAO, J., NEMES, A., LO JACONO, D. & SHERIDAN, J. 2018*c* Branch/mode competition in the flow-induced vibration of a square cylinder. *Phil. Trans. R. Soc. Lond. A* **376**, 20170243.

ZHAO, J., THOMPSON, M.C. & HOURIGAN, K. 2022*a* Damping effect on transverse flow-induced vibration of a rotating circular cylinder and its implied energy harvesting performance. *Phys. Rev. Fluids* **7** (2), 023905.

ZHAO, J., THOMPSON, M.C. & HOURIGAN, K. 2022*b* Decomposition of fluid forcing and phase synchronisation for in-line vortex-induced vibration of a circular cylinder. *J. Fluid Mech.* **941**, R4.

https://doi.org/10.1017/jfm.2025.10866 Published online by Cambridge University Press